Tectonics

RESEARCH ARTICLE
10.1029/2022TC007378

Key Points:
- Pure thrusting and inverted normal faults are described and interpreted
- Analog models are performed to compare with the Domeyko Cordillera as a natural case
- Decapitation of inverted normal faults by thrusting is proposed as first-order structural mechanisms in the Domeyko Cordillera

Correspondence to:
C. López,
cristopher.lopez@ucn.cl

Citation:
López, C., Del Ventisette, C., Bonini, M., Montanari, D., Maestrelli, D., Martínez, F., et al. (2022). The relationship between inverted normal faults and pure thrusting during the tectonic inversion of the Domeyko Cordillera, northern Chile: Structural and seismic interpretation and analog modeling experiments. *Tectonics*, *41*, e2022TC007378. https://doi.org/10.1029/2022TC007378

Received 9 MAY 2022
Accepted 18 NOV 2022

Author Contributions:
Conceptualization: Cristopher López, Chiara Del Ventisette, Marco Bonini, Domenico Montanari, Daniele Maestrelli
Formal analysis: Cristopher López
Funding acquisition: Fernando Martínez, Rodrigo Riquelme
Investigation: Cristopher López, Fernando Martínez, Rodrigo González, Rodrigo Riquelme
Methodology: Cristopher López, Chiara Del Ventisette, Marco Bonini, Domenico Montanari, Daniele Maestrelli, Fernando Martínez
Project Administration: Fernando Martínez, Rodrigo Riquelme
Software: Cristopher López, Daniela Montenegro, Belén Muñoz, Gabriela Guzmán-Marusic
Supervision: Chiara Del Ventisette, Marco Bonini, Domenico Montanari
Validation: Chiara Del Ventisette, Marco Bonini, Domenico Montanari, Daniele Maestrelli, Rodrigo González
Visualization: Daniele Maestrelli

The Relationship Between Inverted Normal Faults and Pure Thrusting During the Tectonic Inversion of the Domeyko Cordillera, Northern Chile: Structural and Seismic Interpretation and Analog Modeling Experiments

Cristopher López[1], Chiara Del Ventisette[2,3], Marco Bonini[3], Domenico Montanari[3], Daniele Maestrelli[3], Fernando Martínez[4], Rodrigo González[1], Rodrigo Riquelme[1], Daniela Montenegro[1], Belén Muñoz[5], and Gabriela Guzmán-Marusic[1]

[1]Departamento de Ciencias Geológicas, Universidad Católica del Norte, Antofagasta, Chile, [2]Dipartimento di Scienze della Terra, Università di Firenze, Firenze, Italy, [3]CNR-IGG, Consiglio Nazionale delle Ricerche, Istituto di Geoscienze e Georisorse, U.O.S. Firenze, Firenze, Italy, [4]Carrera de Geología, Facultad de Ingeniería, Universidad Andres Bello, Campus República, Santiago, Chile, [5]Departamento de Geología, Facultad de Ciencias Físicas y Matemáticas, Universidad de Chile, Santiago, Chile

Abstract The orogenic growth of the Domeyko Cordillera was induced by a positive tectonic inversion. In this work, we have validated this interpretation from new field data, which were combined with 2-D reflection seismic profile interpretations obtained along the Central Andes forearc of northern Chile. To compare with this information, we performed a new series of Analog Models dealing with positive tectonic inversion. On the basis of this, we propose an integrated kinematic model that describes the relationships between extensional structures, inversion structures, and pure thrust faulting. The proposed model is developed with an initial syn-rift phase related to the filling of half-graben basins, followed by a positive tectonic inversion phase. Our models show two main structural styles: partially inverted normal faults and newly formed pure thrust faulting. The partial inversion of previous normal faults represents the initial stage of exhumation of the syn-rift deposits. The pure thrusting consists of east-verging faults, which decapitate early or partially inverted normal faults. The first type of structures are compared with west-verging inverted, or partially inverted, normal faults, inversion anticlines, and buttressing structures, exposed on the western flank of the Domeyko Cordillera. The second type of structures are compared with the east-verging thrust faults exposed on the eastern flank of the Domeyko Cordillera. Finally, we consider that the architecture of the Domeyko Fault System is associated with inversion structures and pure thrust faulting; being these faults first-order structures that led to the orogenic growth of the Domeyko Cordillera from the Upper Cretaceous.

1. Introduction

Deformational mechanisms associated with orogenic growth are not conditioned by a simple convergence-process of an oceanic plate subducted beneath a continental plate (e.g., Andean Orogen; Allmendinger et al., 1997; Dewey & Bird, 1970; Isacks, 1988; Oncken et al., 2006; Ramos, 2010; Scheuber et al., 1994) nor by an accretion of continental blocks (e.g., Himalayan Orogen; Dewey & Bird, 1970; Gavillot et al., 2018; Jain et al., 2012; Valdiya & Sanwal, 2017; Yin, 2006). Specifically, for subduction-related orogens, different studies have proposed that a first-order control corresponds to the absolute motion of the tectonic plates (oceanic vs. continental), inducing, either the retreat of the trench-hinge away from the upper plate (generating an extensional regime), or the advance of the trench-hinge from the upper plate toward the oceanic plate (generating a contractional regime) (Oncken et al., 2006; Ramos, 1999, 2010; Royden & Burchfiel, 1989). In turn, the absolute motion is dependent on the characteristics of the subducting oceanic plate, such as the length of the subduction zone, the convergence rate, the age, and the angle of the subducted or roll-back plate, among others (e.g., Daly, 1989; del Rey et al., 2016, 2019; Doglioni et al., 2009; Jarrard, 1986; Oncken et al., 2006). Nevertheless, the shape of the basins, the stratigraphic geometries, and the internal structures of the orogens (thick- and thin-skinned tectonics) are not exclusively controlled by the subduction- or continental collision-process (Isacks, 1988; Ramos, 2010). Pre-orogenic basement fabrics, such as ancient suture zones, previous normal faults, and zones of cortical weakness by magmatic arcs, exert a strong control on the internal architecture-geometry of orogens (Bonini et al., 2012; Martínez, López, & Parra, 2020; R. W. Butler et al., 2006). Specifically, special attention has been

Writing – original draft: Cristopher López
Writing – review & editing: Cristopher López, Chiara Del Ventisette, Marco Bonini, Domenico Montanari, Daniele Maestrelli, Fernando Martínez, Rodrigo González, Rodrigo Riquelme, Daniela Montenegro, Belén Muñoz, Gabriela Guzmán-Marusic

given to the influence of structures induced by "positive tectonic inversion" on the progressive development of the orogens and fold-and-thrust belts (e.g., Amilibia et al., 2008; Bailey et al., 2002; Bonini et al., 2012; Hayward & Graham, 1996; Martínez, Kania, et al., 2020; McClay & Buchanan, 1992; Williams et al., 1989, among others) (e.g., inversion anticlines, shortcuts, back-thrusts, by-pass faults, or thrust ramps decapitating early normal faults). These structures accommodate a significant amount of the tectonic shortening, exposing large blocks of deeper crust at the surface, generating a greater cortical uplift (Bonini et al., 2012). The tectonic inversion of inherited normal faults has been recognized for many orogens worldwide as being considered one of the most efficient mechanisms acting in the "initial stages" of the orogens building (Bonini et al., 2012; López et al., 2020; Martínez, López, & Parra, 2020; R. W. Butler et al., 2006). Moreover, during the progressive growth of the orogens, the reactivated normal faults may have been converted in reverse faults and/or decapitated by new thrust faults through a "thrust decapitation" mechanism (Del Ventisette et al., 2021; Scisciani, 2009; Welbon & Butler, 1992), which frequently accommodates a major tectonic uplift.

In the case of the Central Andes, despite the existence of robust evidence and interpretations of the structural styles induced by positive tectonic inversion (Amilibia et al., 2008; Fuentes et al., 2018; Martínez, Kania, et al., 2020; Martínez, López, & Parra, 2020; Martínez et al., 2019), the geometry and kinematics of "inherited normal faults," "inversion structures" and "pure thrust faults" are still poorly understood. An example where this relationship has not been clearly interpreted is the Domeyko Cordillera. The Domeyko Cordillera is an orogenic belt developed mainly over Paleozoic and Mesozoic rocks and exposed on the forearc of the Central Andes, northern Chile (Figure 1). Its structural setting has been interpreted as the result of independent and polyphasic deformational events ranging from the Late Cretaceous to Mio-Pliocene (Maksaev & Zentilli, 1999; Mpodozis & Cornejo, 2012; Mpodozis et al., 1993, among others), where different structural styles have been recognized (Arriagada et al., 2006; Bascuñan et al., 2019; Boric et al., 1990; Jordan et al., 2007; López et al., 2019, 2020; Maksaev & Zentilli, 1988, 1999; Martínez, Kania, et al., 2020; Martínez, López, & Parra, 2020; Mpodozis & Cornejo, 2012; Mpodozis et al., 1993; Niemeyer & Munizga, 2008; Niemeyer & Urrutia, 2009; Pananont et al., 2004; Rubilar et al., 2017). Thus, several structural models for the same area have generated questions and doubts about the mechanism of deformation. These different viewpoints and interpretations generate further debate when proposing evolutionary and integrated structural models on a regional scale, since the main models focus on interpretations of independently faulting. In this context, one interesting question is to understand how the pre-existing basement fabrics have influenced the superposition of the deformation regimes; specifically, what is the mechanism that induced the uplift of the Andean forearc. This is an ongoing debate (Amilibia et al., 2008; Bascuñan et al., 2019; López et al., 2020; Martínez, Kania, et al., 2020; Martínez, López, & Parra, 2020; Mpodozis & Cornejo, 2012), which generates a gap in the knowledge of how the Central Andes was structured. To contribute to this discussion, this work analyzes and interprets field data combined with 2-D reflection seismic profiles. To compare and validate our interpretations, we performed a series of Analog Models addressing positive tectonic inversion. These models suggest a new interpretation of inverted structures observed in many places of the Central Andes of northern Chile, which may be compared with similar structures preserved in orogens worldwide. Specifically, we compare our results with EW-oriented segments along the Domeyko Cordillera, located in the forearc of the Central Andes of northern Chile, aiming to evaluate the role played by positive tectonic inversion process in the structuring of the area.

2. Geological Setting

The Andean Orogen is a classic example of a compressional orogen. Specifically, the tectonic setting of the Central Andes is related to the continuous subduction of oceanic plates (e.g., the Farallon and Nazca plates) beneath the South American continental margin (e.g., Allmendinger et al., 1997; Dewey & Bird, 1970; Isacks, 1988; Scheuber et al., 1994). The angle of subduction, the direction of convergence, and the degree of coupling between the oceanic and continental plates have varied through time, controlling the tectonic regimes, determining the episodes and events of deformation of the Andean Orogen, as well as the development and the migration of magmatic arcs toward different positions of the continental margin (e.g., Auboin et al., 1973; Coira et al., 1982; Folguera & Ramos, 2009; Ramos, 2009, 2010). The forearc region of the Central Andes of northern Chile is located on a subducting segment where the slab subducts at an angle of approximately 30° (normal subduction segment). This segment exhibits north-south oriented morpho-tectonic features which are, from west to east, the Coastal Cordillera, the Central Depression, the Domeyko Cordillera or Precordillera, and the Pre-Andean Basins

10.1029/2022TC007378

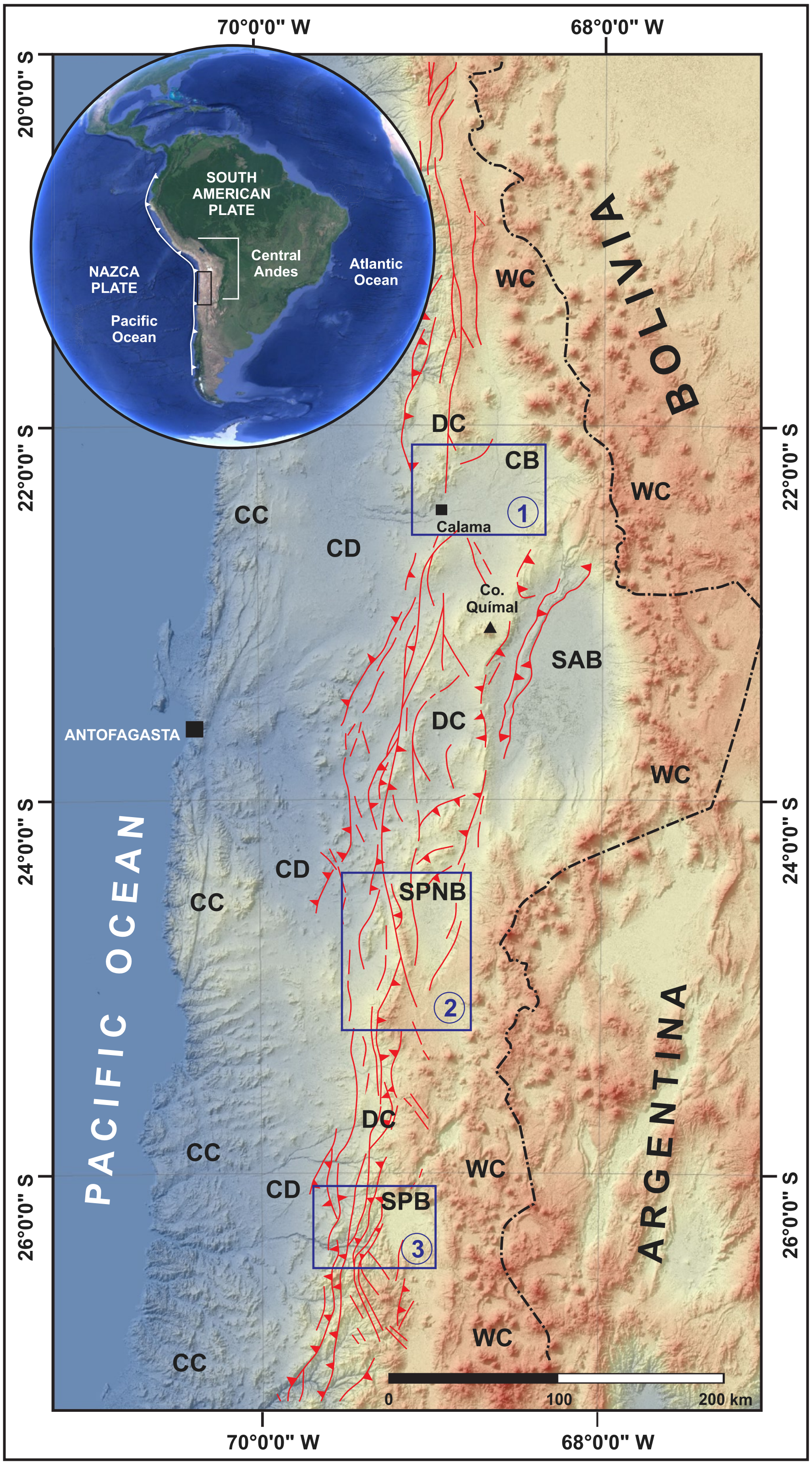

Figure 1. DEM image of the Western Central Andes of South America showing the distribution of the major morpho-tectonic units recognized along northern Chile. CC: Coastal Cordillera. CD: Central Depression. DC: Domeyko Cordillera. CB: Calama Basin. WC: Western Cordillera. SAB: Salar de Atacama Basin. SPNB: Salar de Punta Negra Basin. SPB: Salar de Pedernales Basin. The blue boxes correspond to comparative case studies.

10.1029/2022TC007378

(Cahill & Isacks, 1992; Cembrano et al., 2007) (Figure 1). One of the most prominent morphotectonic features along the forearc region of the Central Andes is the Domeyko Cordillera.

The Domeyko Cordillera is an NNE-oriented and *ca.* 65 km-wide range exposed between 21° and 27°. Its relief is characterized by a westward-inclined flat surface, with an average height varing between 3,000 and 3,500 m above sea level, exposing maximum heights of 4,278 m above sea level (e.g., Cerro Quimal, Figure 1). On the western slope, its structures consist of N-S striking, subvertical, and kilometric-scale faults interpreted as a strike-slip fault system and part of the Domeyko Fault System (Arriagada et al., 2006; Boric et al., 1990; Maksaev & Zentilli, 1988, 1999; Mpodozis et al., 1993; Niemeyer & Urrutia, 2009). Other authors have interpreted the Domeyko Fault System as a clockwise-rotated blocks system with coexist reverse, normal, and strike-slip faults (Mpodozis & Cornejo, 2012). On the other hand, on its eastern slope, east-verging thrust faults bounded the Domeyko Cordillera from the Pre-Andean Basins since the Upper Cretaceous period (e.g., Salar de Atacama, Punta Negra, and Pedernales basins) (Arriagada et al., 2006; Bascuñan et al., 2019; López et al., 2020; Martínez, Kania, et al., 2020; Martínez, López, & Parra, 2020; Niemeyer & Munizga, 2008). Alternatively, other authors propose that the Pre-Andean Depression, at the latitude of the Salar de Atacama, is a product of cortical extension during the Oligocene (Jordan et al., 2007; Pananont et al., 2004; Rubilar et al., 2017) (Figure 1). Other studies, supported by balanced-cross sections (Amilibia et al., 2008), have re-interpreted these structures as inverted faults resulting from the tectonic inversion of pre-existing Mesozoic basement normal faults.

The geological record of the Domeyko Cordillera shows the superimposition of two tectonic settings associated with contrasting geodynamic regimes. The first corresponds to the intracontinental Carboniferous-Lower Cretaceous extensional setting, regionally controlled by roll-back subduction that generated rifting along with the South American margin (Aguirre-Urreta, 1993; del Rey et al., 2016; 2019; Ramos, 2010; Martínez, López, & Parra, 2020; Uyeda & Kanamori, 1979). The depositional record during this period is composed of the Carboniferous to Lower Cretaceous volcanic, fossiliferous marine bioclastic, and siliciclastic stratified rocks (syn-rift deposits), exposed throughout the entire Domeyko Cordillera. In the Calama Basin, the Upper Carboniferous-Permian volcanic sequences are defined as the Collahuasi Formation, the Triassic volcanic and siliciclastic rocks are defined as the Tuina and Quetena Formations, the Jurassic marine and fossiliferous deposits are defined as the Caracoles Group, and the Upper Jurassic-Lower Cretaceous siliciclastic deposits are defined as the Cerritos Bayos Formation (A. J. Tomlinson et al., 2018; Duhart et al., 2018). In the Salar de Punta Negra Basin, the Upper Carboniferous-Permian volcanic sequences are defined as the La Tabla Formation, the Triassic volcanic and siliciclastic rocks are defined as the Sierra de Varas and the Cerro de Guanaco Formations, the Jurassic marine and fossiliferous deposits are defined as the Profeta Formation, and the Upper Jurassic-Lower Cretaceous siliciclastic deposits are defined as the Quebrada Portezuelo and the Cerro Islote Beds (González et al., 2015). Finally, in the Salar de Pedernales Basin, the Upper Carboniferous-Permian volcanic sequences are defined as the La Tabla Formation, the Triassic volcanic and siliciclastic rocks are defined as the Quebrada del Salitre Formation, the Jurassic marine and fossiliferous deposits are defined as the Asientos and the Montandón Formations and the Cerro Vicuñita Beds, and the Upper Jurassic-Lower Cretaceous volcanic and sedimentary rocks are defined as the Sierra Fraga, the Punta del Cobre, and the Pedernales Formations (A. Tomlinson et al., 1999). The second tectonic setting consists of a contractional feature induced by the early Upper Cretaceous to recent contraction of the continental margin related to the eastward trench advance, which caused the shortening and tectonic uplift of the Central Andes forearc (Amilibia et al., 2008; Cobbold et al., 2007; Ramos, 2010). The depositional record during this period is composed of the Upper Cretaceous to Cenozoic volcanic and siliciclastic stratified rocks (synorogenic deposits), exposed mainly in the eastern flank of the Domeyko Cordillera. In the Calama Basin, the Upper Cretaceous-Paleocene volcanic and sedimentary sequences are defined as the Quebrada Mala and Tolar Formations (. J. Tomlinson et al., 2018; Duhart et al., 2018). In the Salar de Punta Negra Basin, the Upper Cretaceous-Paleocene volcanic and sedimentary sequences are defined as the Quebrada Mala and Chile-Alemania Formations (González et al., 2015), and the Eocene-Lower to Lower Miocene conglomerates and gravels are defined as the Pampa de Mula and the Aguada Zorro Formations. Finally, in the Salar de Pedernales Basin, the Upper Cretaceous-Paleocene volcanic and sedimentary sequences are defined as the Llanta Formation and the Eocene-Lower to Lower Miocene conglomerates and gravels are defined as the Atacama Gravels (A. Tomlinson et al., 1999). The contraction was developed diachronically during several deformation events or tectonic phases (e.g., ca. 100–90, 65, and 40 Ma; Arriagada et al., 2008; Bascuñan et al., 2015; Cornejo et al., 2003; Mpodozis & Ramos, 1990; Mpodozis et al., 2005; Somoza et al., 2012; Steinmann, 1929), which were usually accompanied by eastward migration of the magmatic arcs distributed in similar longitudinal positions during Upper Cretaceous to Oligocene times.

3. Methodology

3.1. Surface and Subsurface Structural Interpretations

In order to understand the geometry and kinematics of the relationship between "inverted normal faults" and "pure thrusting or newly formed pure thrust faults" during tectonic inversion, we analyzed three E-W oriented cross-sections located on specific areas of the Domeyko Cordillera. The cross-sections correspond to the Sierra de San Lorenzo-Calama Basin segment (blue box 1-CB, in Figure 1), the Cerro Islote-Salar de Punta Negra Basin segment (blue box 2-SPNB in Figure 1), and the Potrerillos Fold and Thrust Belt-Salar de Pedernales Basin segment (blue box 3-SPB in Figure 1). The cross-sections were made by integrating field and subsurface data. The field data consists of geological maps constructed from the interpretation of satellite images and field observations, integrated with stratigraphic and structural data from the literature (A. Tomlinson et al., 1999; A. J. Tomlinson et al., 2018; Cornejo et al., 2013; González et al., 2015). Geological contacts, strike and dip measurements, stratigraphic thickness, and the position of faults and folds represent the main geological field information. These data were combined with a series of industrial seismic profiles with the vertical axes in time, crossing the above-mentioned Pre-Andean Basins and showing a continuity between some large structures exposed on the surface and regional subsurface structures hidden under the Pre-Andean Basins. The 2-D seismic reflection profiles were provided by the ENAP-Sipetrol exploration team. These were acquired between the 1970s–1990s during the early oil and gas exploration of the Central Andean forearc and have been released for academic and scientific purposes. More details about the processing, quality, and methods of the interpretation of this data can be found in Martínez et al. (2018, 2019) and Martínez, Muñoz, et al. (2021).

3.2. Analog Models

The analog modeling experiments were carried out at the TOOLab (Tectonic Modeling Laboratory), which is a joint laboratory between the Department of Earth Sciences of Firenze and the Istituto di Geoscienze e Georisorse of the Consiglio Nazionale delle Ricerche, Italy. Specifically, the models were deformed under extensional and compressional conditions, inducing a positive tectonic inversion, using a pure/simple-shear deformational apparatus. Our models intend to simulate the tectonic and stratigraphic conditions presented in López et al. (2019, 2020) and Martínez, López, and Parra (2020), which illustrated the geological setting between the Domeyko Cordillera and Pre-Andean Basins as the result of positive inversion tectonics and pure shortening faulting interplays. Particularly, our models simulated the pre-rift Paleozoic basement of the Domeyko Cordillera, as well as (a) syn-rift sedimentation (Late Carboniferous to Mesozoic rocks), (b) post-rift sedimentation (Upper Jurassic-Lower Cretaceous rocks), and (c) syn-shortening sedimentation (Upper Cretaceous-Cenozoic rocks), with which it was possible to test the conditions that could have controlled the tectonic evolution of the case study under consideration.

3.2.1. Experimental Setup

For the initial setup, an acrylic box with 1 cm-thick walls and internal dimensions of 25 cm × 25 cm × 6 cm was used. It was placed on a rigid stainless-steel table which served as support and for the positioning of plates simulating the direction of shortening or extension (Figure 2a). One of these plates corresponded to a rigid immovable steel wall (fixed wall), while the extension and shortening were induced by a mobile wall (Figure 2a) controlled by a stepper motor. The mobile wall was connected at the base to a plastic rectangular sheet (<1 mm thick) below a basal ductile layer of polydimethylsiloxane (PDMS), inducing a basal velocity discontinuity (VD): it was used to convert the motion of the mobile wall into a basal stretching of the PDMS layer, that is, inducing a model deformation (Figure 1d). The VD was active only during the extensional phase, and disconnected during the compressive phase. The shortening and extensional velocity was operated through a control console (Figure 2b).

During the model deformation, we acquired high-resolution (10MP) top-view photos (every 2 min intervals) through a reflex camera (Canon EOS 1100D) mounted vertically above the model surface. Also, high-resolution (10MP) section-view photos were acquired for all final cross-sections obtained from the models.

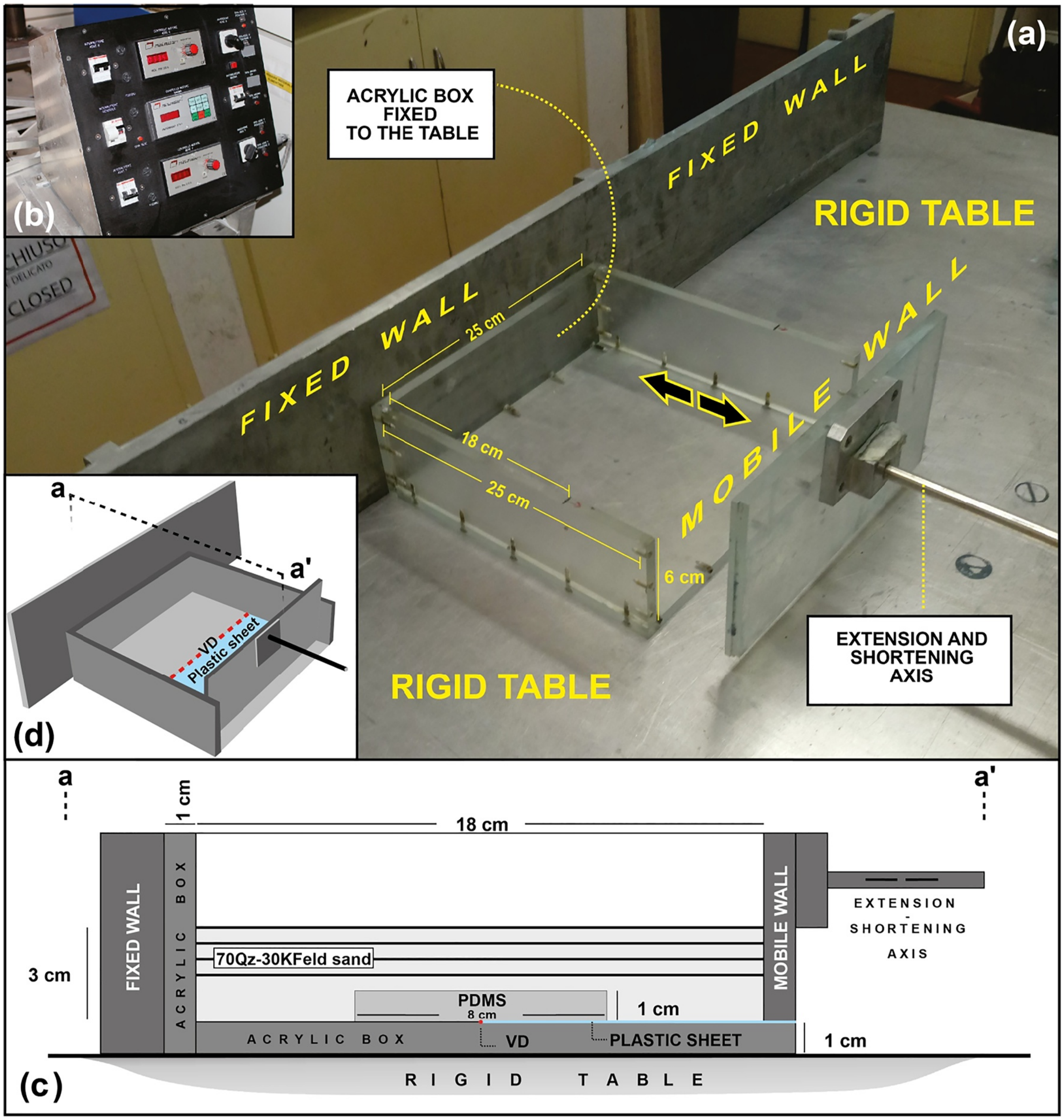

Figure 2. Facilities and equipment used during the performance of the analog modeling experiments in the Tectonic Modeling Laboratory. (a) Initial preparation of the acrylic box on the rigid table that will serve as a support for the modeling. (b) Control console. (c) The aa′ cross-section representing the setup setting to run the analog models. (d) Scheme showing the plastic sheet and the position of the VD and the aa′ representative cross-section. PDMS: polydimethylsiloxane. VD: basal velocity discontinuity.

Analog models underwent two deformation phases: (a) a first extensional phase (with or without syn-rift sedimentation) followed by (b) a shortening phase (positive tectonic inversion). To better characterize and analyze the extensional geometries, the first two models were stopped after the extensional phase. The summary of the characteristics and parameters for each model carried out is presented in Table 1.

1. Initial setup (basal pre-rift sand) and extensional phase (syn-rift sedimentation): In the first phase, the models focused on an initial orthogonal (Figure 2c) extensional phase (i.e., extension was applied orthogonally to the VD and to the trend of the PDMS layer). The initial setup consisted of a 3 cm-thick brittle sequence (pre-rift basal sand) composed of 70% quartz sand and 30% K-feldspar sand (70Qz-30Feld; Figure 2c). Before incorporating the basal sand, a 1 cm-thick, 25 cm-long, and 8 cm-width ductile PDMS silicone layer was centrally positioned on top of the VD, with an orthogonal arrangement to the direction of extension or shortening

10.1029/2022TC007378

Table 1
Summary Table of the Analog Models Presented in This Study

Model	Type	PDMS (cm)	Extension velocity (mm/hr)	Amount of extension (cm)	Syn-rift sedimentation	Extension time (min)	Post-rift sedimentation	Shortening velocity (mm/h)	Amount of shortening (cm)	Syn-shortening sedimentation	Shortening time (min)
ATM_01	Pure extension	8	25	2,0	–	50	–	–	–	–	–
ATM_02	Pure extension	8	25	4,0	ys,bs,bcks,lbs,ys,bcks	91	–	–	–	–	–
ATM_03	Positive inversion	8	25	2,3	–	50	only ys and ws	25	2,3	–	50
ATM_04	Positive inversion	8	25	2,5	ys,bs,bcks,lbs,ys,bs,ws	55	–	25	2,5	–	58
ATM_05	Positive inversion	8	25	2,2	ys,bs,bcks,lbs,ys	49	–	25	2,7	ws,bcks,ws,bcks,ws, ys,bs,bcks,lbs,ys	55
ATM_06	Positive inversion	8	25	2,5	ys,bs,bcks,lbs,ys	50	–	50	4,0	ws,bcks,ws,ys,bs,bcks,lbs,ys,bcks	44
ATM_07	Positive inversion	8	25	2,5	ys,bs,lbs,ys,bs,ys	58	ws,bs,ws,bs,ws	25	2,5	ys,bs,lbs,bs,ys,bs	58

Note. The parameters and characteristics for each model made are shown. The colored sands for each sedimentation phase are indicated: ys = yellow sand; bs = blue sand; bcks = black sand; lbs = light blue sand; ws = white sand.

(Figure 2c). An extensional velocity of 25 mm/hr was applied to the moving wall, for 60 min, implying an extension of 2.5 cm.

2. Shortening phase: Similarly, in this second phase, the models were deformed under coaxial and orthogonal shortening (i.e., parallel to the direction of extension applied in the first phase and therefore orthogonal to first phase-related normal faults). The deformation velocity was 25 mm/hr generating an approximate shortening of 2.5 cm (although it was varied depending on the model, see Table 1). However, the models also considered the effect of velocity-variability, increasing it during this phase (velocity was double; i.e., 50 mm/hr for model ATM_06; Table 1). The velocity increasing can significantly change the coupling between ductile and brittle layers, which in turn can control the style of deformation in the final model (e.g., Brun, 2002).

The analog modeling also reproduced, for each phase, the different sedimentation associated with various tectonic regimes, namely, (a) syn-rift, (b) post-rift, and (c) syn-shortening sedimentations.

1. *Syn-rift sedimentation:* this sedimentation involves the incorporation of layers of colored K-feldspar sand, during the extensional phase (5 or 6 layers depending on each model). It was applied every 4 min intervals, starting from minute 18 after onset of deformation. The choice of this time interval allowed for a final syn-rift sedimentation thickness approximately 1 cm, correctly scaling to an approximate natural thickness of 1 km (see Section 3.2.2 for details).
2. *Post-rift sedimentation:* this sedimentation was incorporated when the model stopped, once the extensional phase finished, and before the beginning of the shortening phase. It involved layers of blue and white K-feldspar sand. The post-rift sedimentation reached an estimated total thickness varying between 0.5 and 0.8 cm.
3. *Syn-shortening sedimentation:* this sedimentation incorporated layers of fine colored K-feldspar sand (5 or 8 layers depending on the model). Sedimentation was applied every 4 min and started at minute 18, at the beginning of the shortening phase. Syn-shortening sediment reached a total thickness of approximately 1 cm, being applied evenly throughout the entire model.

3.2.2. Materials and Scaling

To simulate the brittle pre-rift basement, we used a mixture of quartz sand (Fontainebleau quartz sand; Qz-sand) and K-feldspar fine sand (Kaolinwerke-AKW feldspar FS 900 SF sand; K-feldspar sand) with proportions of 70:30 in weight. The obtained Mohr-Coulomb granular material has a bulk density of 1,408 kg m^{-3}, an angle of internal friction of ∼40°, a coefficient of friction $\mu \sim 0.83$ and cohesion of ∼10 Pa (material parameters have been characterized through empirical methods; see Del Ventisette et al. (2019) and Montanari et al. (2017) for extensive description of the adopted methods). The sand mixture was placed in a pack with different intercalations of gray sand layers used as passive markers to visualize the internal deformation in the final cross-sections. A basal ductile layer of PDMS was introduced in the models, as both a technical solution to distribute deformation and to simulate the potential intra-crustal detachment layers. PDMS is a transparent Newtonian silicone, with a density of 965 kg/m^3, and a viscosity of $\sim 5 \times 10^4$ Pa s (e.g., Weijermars, 1986). In order to reproduce the mechanical stratigraphy of the study area, syn-rift, post-rift, and syn-shortening sedimentation were simulated using an alternation of different colored layers of pure K-feldspar sand (Kaolinwerke-AKW feldspar FS 900 SF), which has a bulk density of ~1,000 kg m^{-3}, an angle of internal (peak) friction of 59°, a coefficient of friction $\mu \sim 1.73$ and cohesion of ~12 Pa (Del Ventisette et al., 2019; Montanari et al., 2017). Despite its slightly higher cohesion with respect to the sand mixture used to simulate basement rocks (Qz-Kfeld 70:30), the K-feldspar sand was chosen to represent the syn-rift to syn-shortening deposition due to its low bulk density. K-feldspar sand was sieved homogeneously on the model surface, reaching a uniform thickness of ~1 mm on the undeformed areas, while it increased proportionally in depocentres (thickness was checked through transparent plexiglas box sidewalls).

Models were scaled to nature to achieve geometric and dynamic similarity (Hubbert, 1937; Ramberg, 1981). We used an appropriate length scaling ratio (l^*, with the asterisk denoting the ratio between the model and the natural prototype) of 10^{-5}. This implies that 1 cm in the models corresponds to 1 km in nature. Consequently, the scaling ratio of stress (σ^*) can be obtained from $\sigma^* = l^*\, g^*\, \rho^*$, where g is the gravitational acceleration, and ρ is the rock density. Considering that $g^* = 1$ (i.e., both model and prototype are experiencing the same gravitational acceleration) and ρ^* is ~0.53, the resulting stress scaling ratio σ^* is of the order of ~5.41×10^{-6}. Kinematic similarity can be addressed by scaling down to nature of the viscous PDMS layer. Considering a viscosity (η_m) of ~5×10^4 Pa s for the PDMS and an average natural viscosity (η_n) ranging between 10^{19} and 10^{21} Pa s (e.g., Weijermars, 1986), we obtain a viscosity scaling ratio ($\eta^* = \eta_m/\eta_n$) of 10^{-15}–10^{-17}.

The velocity scaling ratio can be calculated through $V^* = \varepsilon^*\, l^* = (\sigma^*\, l^*)/\eta^*$. Assuming a modeling velocity (V_m) of 25 mm hr^{-1}, we therefore obtain scaled natural velocities ranging between 0.2 and 20 mm yr^{-1}, which are in good agreement with velocity range of natural extensional settings and compressional thrust systems (e.g., Kukal, 1990).

Finally, it is worth mentioning that, as it normally occurs in analog modeling, common methodological limitations are associated with our models (see Schellart & Strak, 2016). For example, an important limitation of our models is the approximation of thermo-mechanical processes associated with extensional and compressional setting to purely mechanical processes. Nonetheless, being our models performed at shallow crustal scale, the relevance of this effect is somehow reduced.

4. Description of Surface Structures

4.1. Sierra de San Lorenzo-Calama Basin Segment

A limited number of structures have been recognized on the western most part of the Calama Basin (blue box 1-CB in Figure 1). Along the San Salvador River Canyon and the Cerros de Quetena (ca. 22°20′–22°29′ Lat. S) (Figure 3a), the main structure consists of a west-dipping monocline involving stratified sequences ranging from the Carboniferous-Permian to the Upper Jurassic units (Collahuasi Fm., Tuina Fm., Caracoles Gr., Cerritos Bayos Fm., respectively; A. J. Tomlinson et al., 2018; Duhart et al., 2018) (Figures 3b and 4a). Specially, the Jurassic successions exhibit wedge-shape syn-rift deposits thicker to the west where they are folded, and are locally affected by subsidiary normal faults (Figure 4c). At the Cerro Quetena, on the west part of the Calama Basin (Figure 4b), a west-verging thrust fault system controls the location of the Jurassic and Triassic deposits (Caracoles Gr. And Collahuasi Fm, respectively) at the surface. We described this thrust system as a break-back thrust sequence (*sensu* R. W. H. Butler, 1987) (Figure 4b). These faults would provide the pathway for the emplacement of some magmatic bodies, since the Eocene intrusive rocks are put in contact with Jurassic deposits through thrust faults (Figure 4d). Furthermore, these thrusts would be part of an antithetic fault system to the main structural domain, that can be recognized in EUCC91-04 seismic profile (see Figure 10). To represent and highlight the first-order structures, we constructed a generalized E-W oriented cross-section (Figure 3b), considering the structural characteristics recognized in the western border of the Calama Basin. In this profile, an east-verging hanging-wall anticline is depicted. This type of structure would be associated with a fault-bend fold related to a ramp-flat-ramp geometry in depth. In the Calama Basin, the detachment fault is below the cover of recent sedimentary basin infill, and can be imaged and correlated in a EUCC91-04 seismic profile (see next section). This fault would trend approximately NE and would limit the main positive topographic features of the northwestern part of the basin.

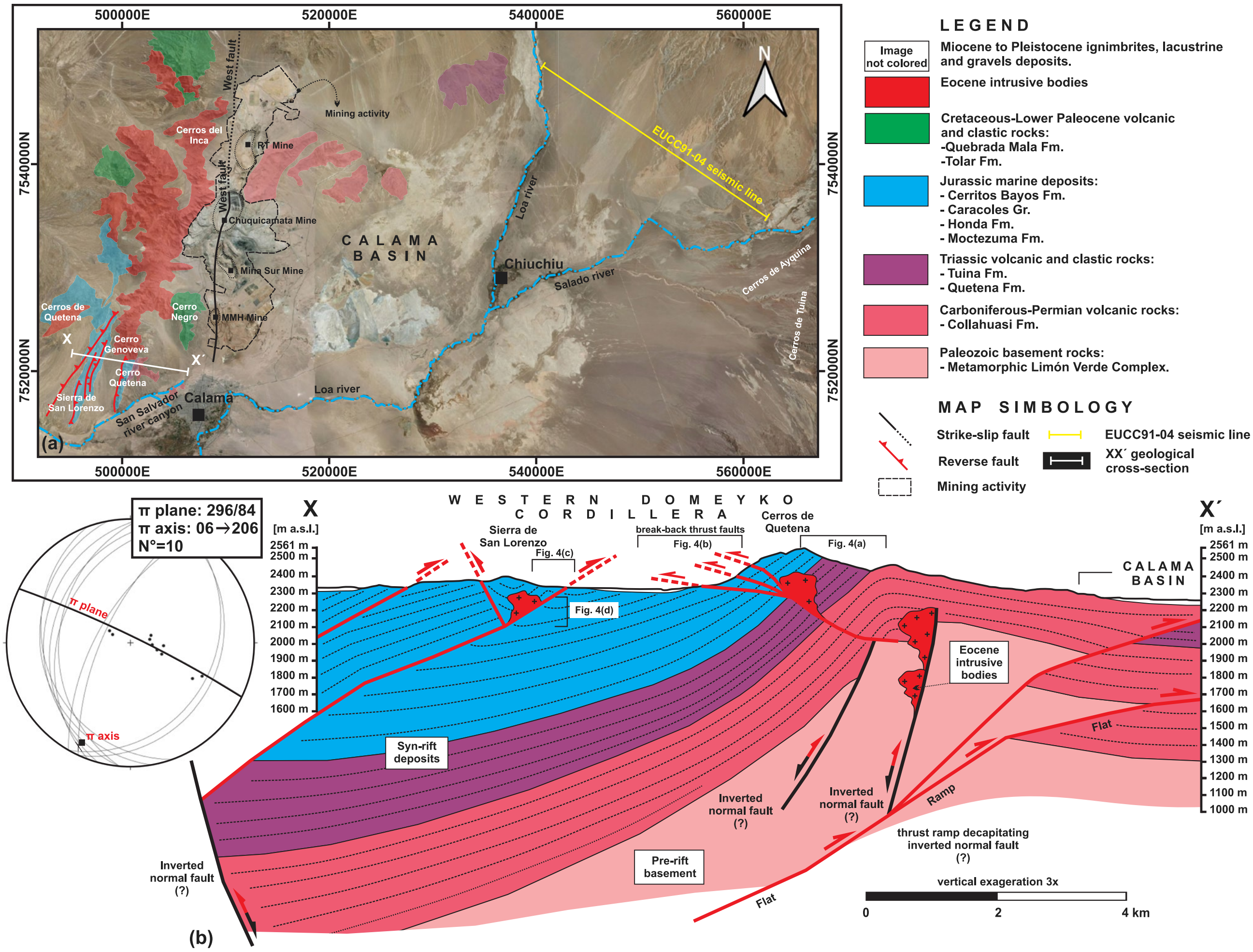

Figure 3. (a) Generalized geological map of the Calama Basin area and (b) XX′ geological cross-section. The stereographic projection shows the orientation of planes and poles (black points) of measured bedding obtained from the stratigraphic units recognized along the XX′ geological cross-section and its respective fold analysis (π corresponds to the fold axis). In panel (a), the location of the EUCC91-04 seismic line and XX′ geological cross-section presented in this study are shown. Modified from Tomlinson et al. (2018). The XX′ cross-section is located between the Sierra de San Lorenzo and Calama Basin and the relationship between deposits and its structural control stand out.

4.2. Cerro Islote-Salar de Punta Negra Basin Segment

The main structures are exposed in the Cerro Islote, the Sierra Vaquillas Altas, and the Sierra de Varas (blue box 2-SPNB in Figure 1) located on the easternmost part of the Domeyko Cordillera (ca. 24°30′–25°30′ Lat. S) (Figure 5a). In plain view, N-S striking bedding and doubly verging thrust faults are recognized, involving and exhuming both the Paleozoic crystalline basement rocks and the Upper Paleozoic and Mesozoic stratigraphic sequences. The structural styles identified in this region are represented in a schematic E-W oriented cross-section, where they show the relationship between thick-and-thin-skinned folds and faults (Figure 5b). Initially, toward the westernmost and central parts (i.e., Cerro Islote and Sierra de Vaquillas Altas, respectively), N-S striking narrow and upright anticlines-synclines are well exposed involving Triassic-Lower Jurassic marine syn-rift deposits (Profeta and Quebrada del Salitre formations). Here, doubly verging thin-skinned folds and thrusts related to intraformational detachment are the result of a buttressing effect (Figure 6). These folds involve syn-rift strata and are kinematically associated with inversion anticlines-syncline created from the partial positive reactivation of an early east-dipping Upper Paleozoic-Mesozoic normal fault (Figure 6c). Evidence of tectonic inversion is recognized along the Vaquillas Creek. In these outcrops, partially inverted east-dipping normal faults, involving the Triassic and Jurassic syn-rift deposits, are preserved under the Cenozoic gravels

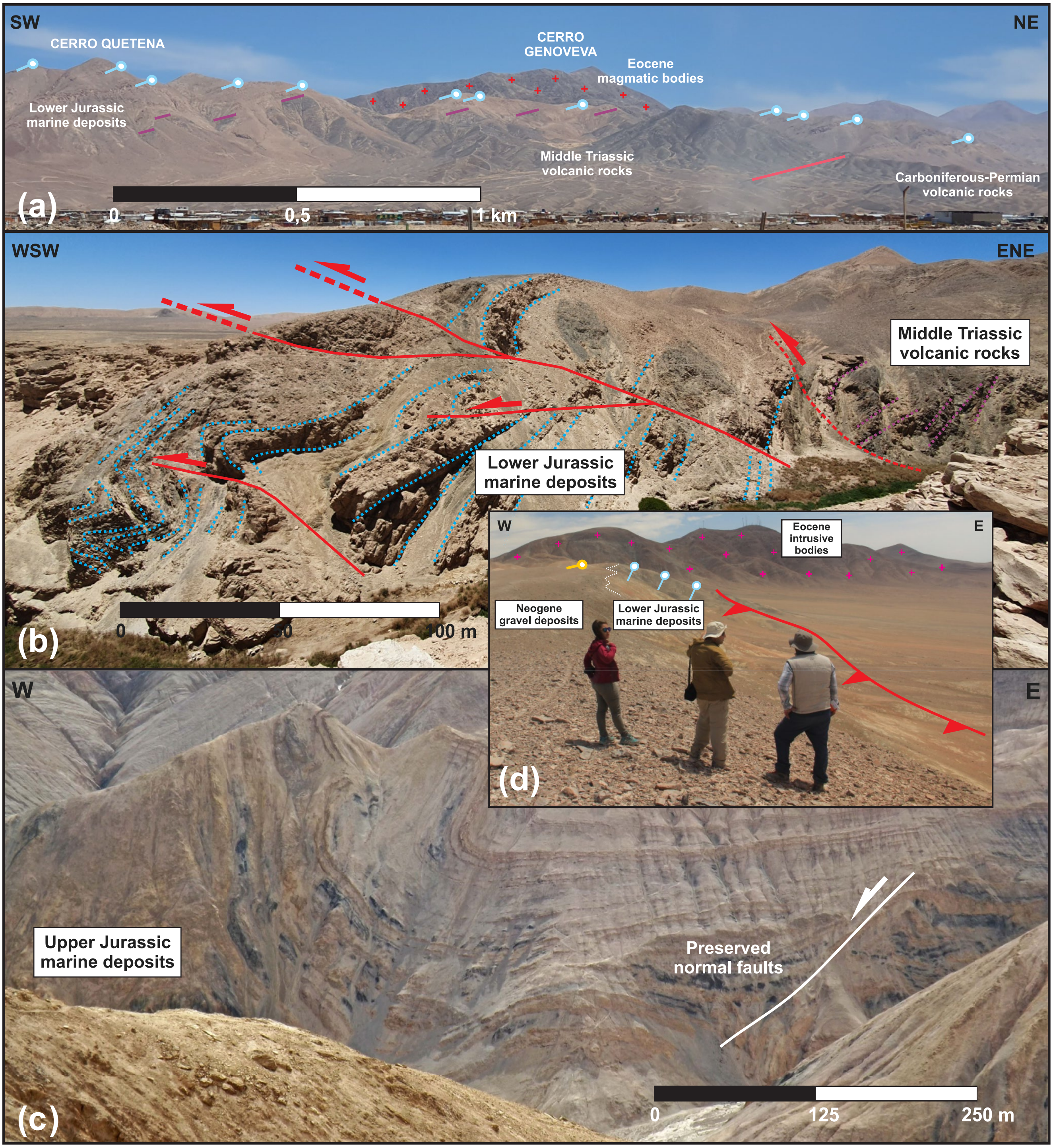

Figure 4. Some first-order structural styles exposed on the Domeyko Cordillera to the west of the Calama Basin. (a) West-dipping Carboniferous-Permian to Jurassic monocline outcropping on the Sierra de San Lorenzo. (b) Break-back thrust sequence. (c) Syn-rift wedge geometry involving to the Jurassic sequences. (d) Thrust fault as mechanism of the emplacement of the Eocene magmatic body.

(Figure 7a). Some inversion-related faults, such as short-cut and back-thrust faults, are recognized as the result of the inversion of half-graben basins (Figures 7b and 7c). The frontal limbs of the folds and the uppermost part of the reactivated normal fault are unconformably overlain by the Upper Cretaceous-Paleocene synorogenic clastic and volcanic deposits (Quebrada Mala and Chile-Alemania Fms.), thus constraining the timing of late

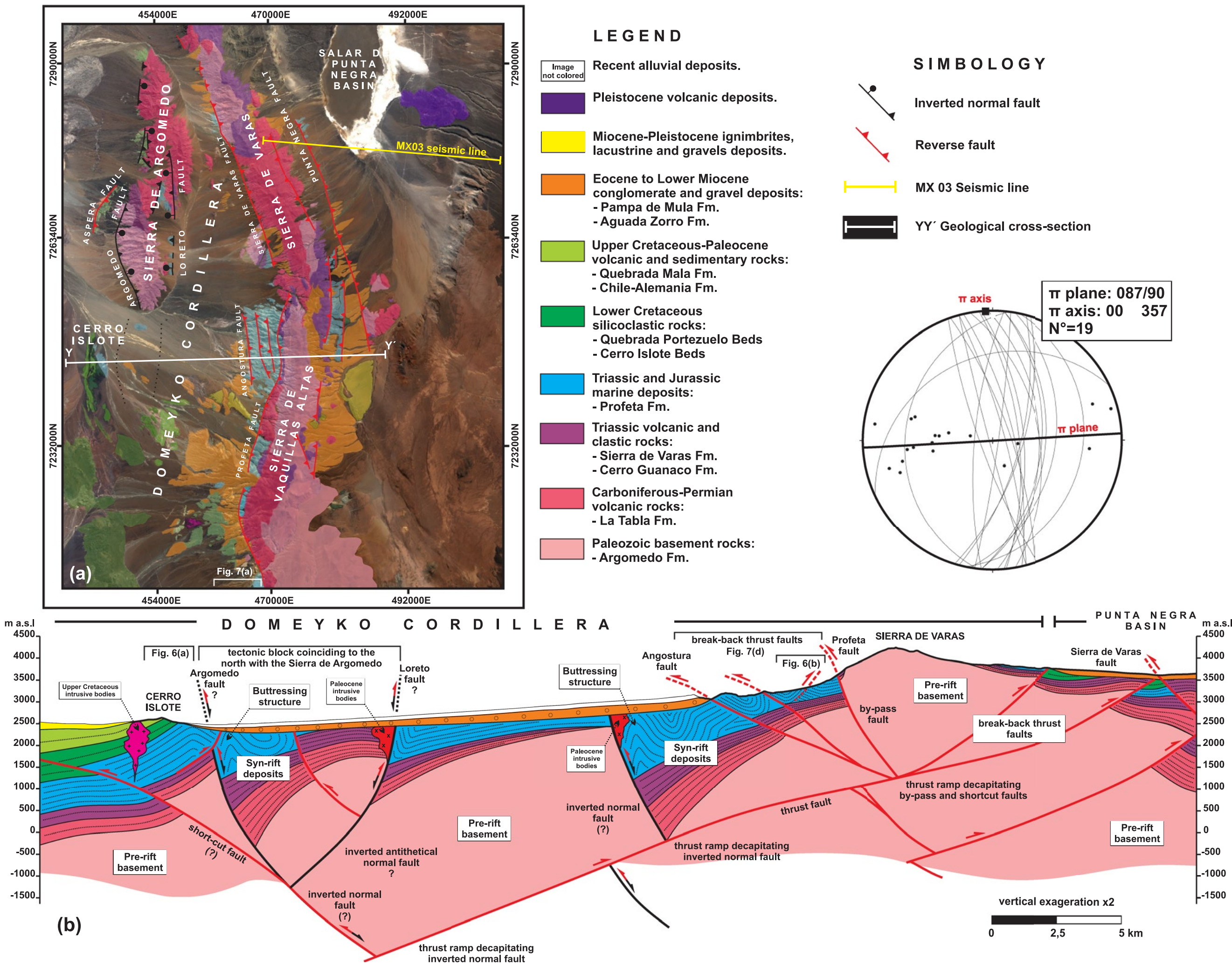

Figure 5. (a) Generalized geological map of the Sierra de Varas and Salar de Punta Negra Basin and (b) the YY′ cross-section area. The stereographic projection shows the orientation of planes and poles (black points) of measured bedding obtained from the stratigraphic units recognized along the YY′ geological cross-section and its respective fold analysis (π corresponds to the fold axis). The location of the MX03 seismic line and YY′ cross-sections presented in this study are shown. Modified from González et al. (2015). The YY′ geological cross-section is located between the Cerro Islote-Salar de Punta Negra Basin; the relationship between deposits and its structural control stand out.

Cretaceous contraction (Figures 6a and 6c). Immediately toward the east of the Cerro Islote and to the western slope of the Sierra de Varas, the Upper Cenozoic gravels and volcanic deposits are widely exposed over a *ca.* 24 km-wide region. These deposits overlie through a marked angular unconformity (thus hiding) the Triassic-Upper Jurassic folded and thrusted deposits (Figure 6b). Nevertheless, to the north, the flat surface of gravel deposits is interrupted by the Sierra Argomedo, which is controlled by two opposite-vergence thrust faults (Figures 5a and 5b). To the west, the Argomedo fault is an example of an east-dipping inverted normal fault; while to the east, the Loreto fault corresponds to an inverted antithetic normal fault (Figure 5b). Both faults generate different exhumation levels of the pre-rift basement and syn-rift deposits, which are also accompanied by depositional and deformational geometries related to positive tectonic inversions of the rift basins. Finally, toward the easternmost part of the cross-section, the structural style is mainly thick-skinned, composed of N-trending and doubly verging thrust faults well exposed on the west and eastern flanks of the Sierra de Varas. On its western flank, two-parallel west-vergence thrust faults are related to the extrusion and exhumation of the Carboniferous-Permian and Triassic-Jurassic syn-rift deposits through "break back-thrust faults," placing them in contact with the Neogene gravels deposits (Figures 5b and 7d).

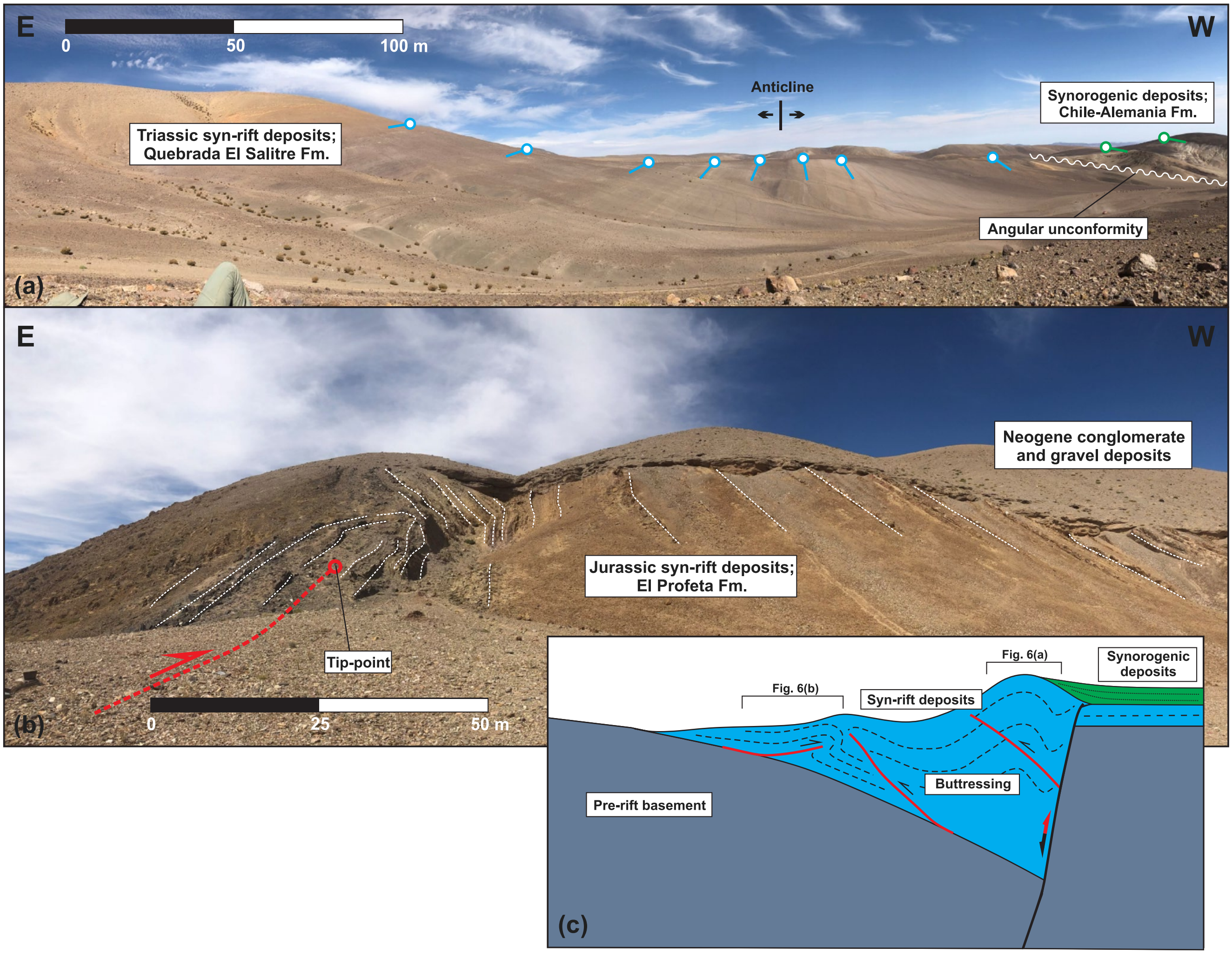

Figure 6. Buttressing structures. (a) Buttressing fold involving Triassic syn-rift deposits underlying the Paleocene synorogenic deposits. (b) Detachment fold involving Jurassic syn-rift deposits. (c) Idealized model of a buttressing structure with main structures and depositional geometries standing out.

4.3. Potrerillos Fold-and-Thrust Belt and Salar de Pedernales Basin Segment

To show the main structures highlighted in this segment (blue box 3-SPB in Figure 1), we constructed a simplified E-W-oriented cross-section located between the Llano San Juan and Pedernales Basin (Figure 8b). Here, three different structural styles are well-exposed along with the Quebrada del Salado canyon (Figure 9). First, normal faulting and depositional geometries related to an extensional regime are recognized. These faults consist of inherited, N-striking and east-dipping normal faults. Its hanging-wall involves syn-rift deposits, which usually show wedge shapes and are thicker close to the fault planes (Figures 9a and 9b). The syn-rift wedges mainly involve the Carboniferous-Permian to Lower Cretaceous sedimentary and volcanic rocks (Figure 9c). Another structural style consist of a hybrid NNE-striking and east-verging thin and thick-skinned thrust belt referred to as the Potrerillos Fold and Thrust Belt, which affects the Carboniferous-Permian to Miocene sedimentary and volcanic rocks (Figure 8). From west to east, the Barrancas fault consists of a west-dipping thrust fault that superposes the pre-rift basement Paleozoic granitic rocks (Sierra Castillo Batholith) onto Mesozoic deposits (Montandón and Asientos Formations and Cerro Vicuñitas Beds) which are involved in an asymmetrical footwall syncline (the Guanaco Muerto syncline; A. Tomlinson et al., 1999) (Figure 8b). Immediately to the east, the Río de La Sal, the El Choclo, and the El Buitre faults may be defined as a thin-skinned thrust system affecting mainly the Upper Jurassic to Lower Cretaceous syn-rift sequence (Figure 9c). Within this system, the El Choclo fault defines a “fault-bend fold geometry,” in which an east-verging hanging-wall anticline is exposed (Figure 9d). Finally, another first-order structure is the Sierra Castillo fault, which has commonly been defined as a steeply

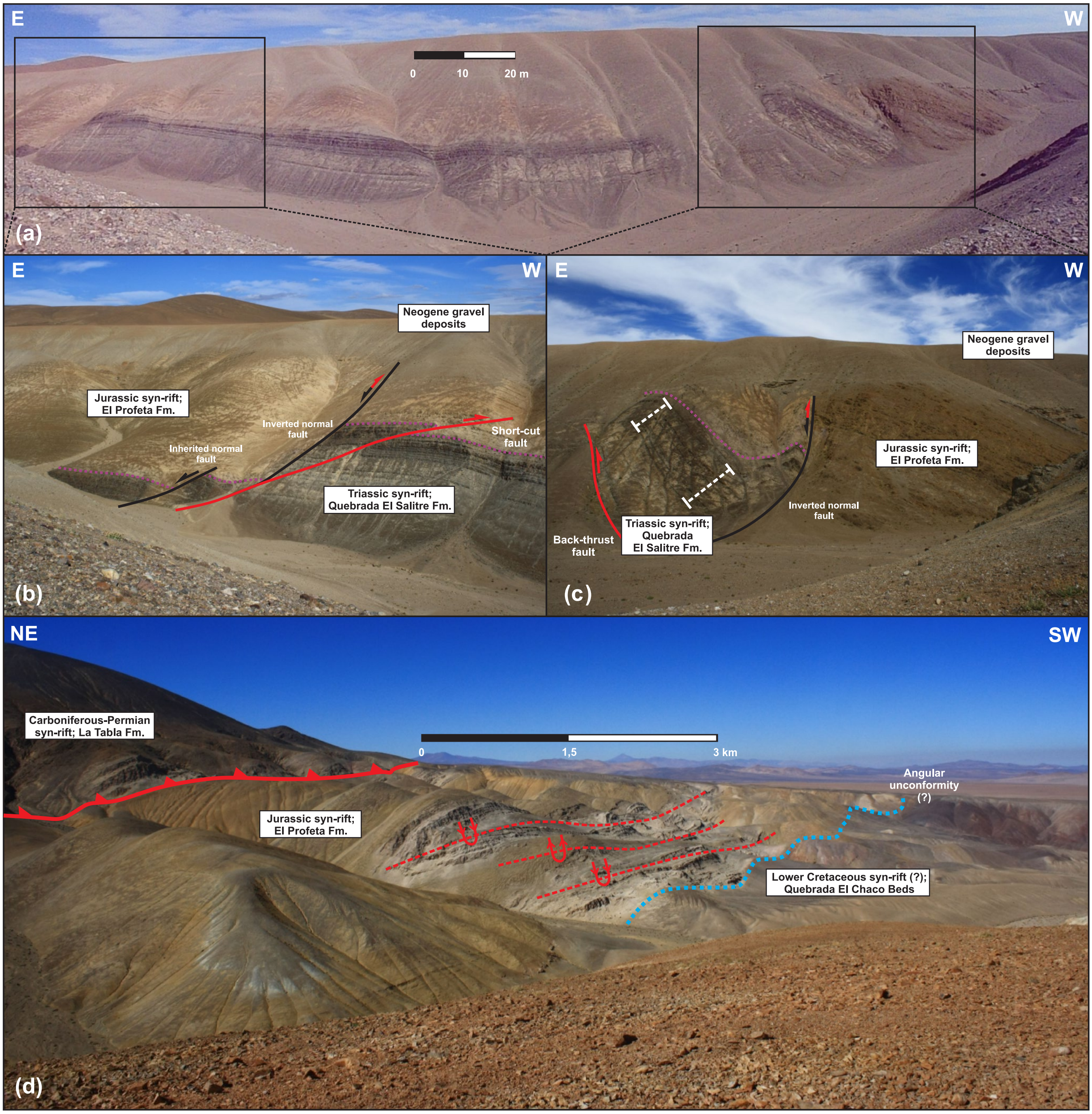

Figure 7. Inversion structures. (a) The Vaquillas Creek exposing Triassic and Jurassic outcrops. (b) Partially inverted normal fault and short-cut fault. (c) Partially inverted normal fault and back-thrust fault. (d) West-vergence thrust fault raising the Carboniferous-Permian volcanic rocks (hanging wall) over the Jurassic marine deposits (footwall).

dipping strike-slip fault, juxtaposing Paleozoic crystalline rocks (pre-rift basement), to the east, with Middle Jurassic-Lower Cretaceous sedimentary and volcanic rocks, to the west (A. Tomlinson et al., 1999; Niemeyer & Munizga, 2008). The Sierra Castillo fault represents a structural boundary, separating two domains. To the east, east-verging thrust faults are the main structures (e.g., the Potrerillos fold and thrust belt), whereas to the west, a minor west-verging thrust fault system controls the western slope of the Domeyko Cordillera. In the latter domain, the Kilómetro Catorce and Sierra Los Sapos faults affect Cretaceous volcanic and sedimentary rocks exposed and limited to the western slope of the Domeyko Cordillera. Based on the observation that these thrust

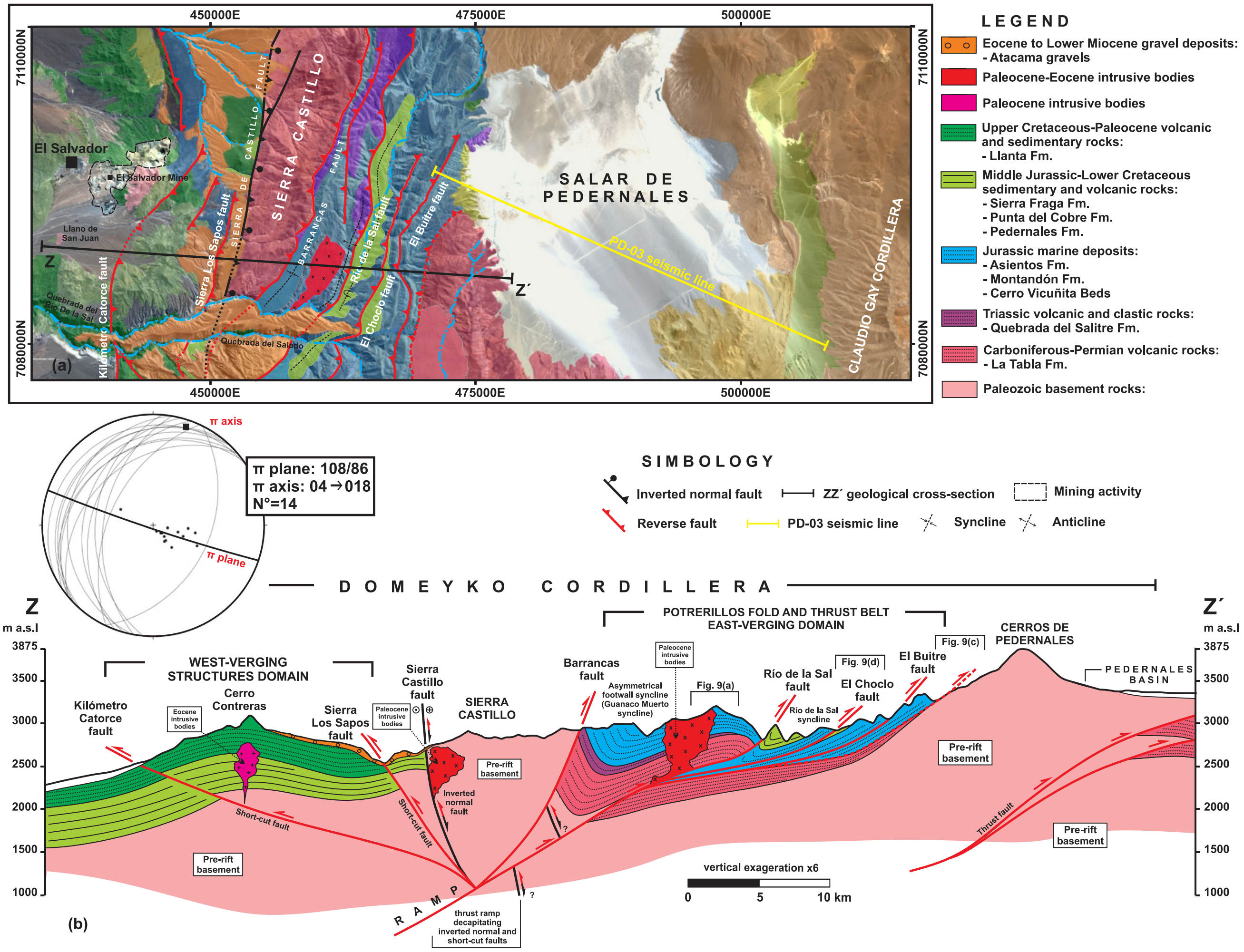

Figure 8. (a) Generalized geological map of the Potrerillos Fold and Thrust Belt and Salar de Pedernales Basin area and (b) the ZZ′ geological cross-section. The stereographic projection shows the orientation of planes and poles (black points) of measured bedding obtained from the stratigraphic units recognized along the ZZ′ geological cross-section and its respective fold analysis (π corresponds to the fold axis). The location of the PD-03 seismic line and ZZ′ geological cross-sections presented in this study are shown. Modified from Tomlinson et al. (1999). The ZZ′ geological cross-section is located between the Potrerillos Fold and Thrust Belt and the Pedernales Basin.

faults are exposed to the west of the Sierra Castillo fault, both the Kilómetro Catorce and Cerro Contreras faults may be considered as short-cut faults linked to the positive tectonic inversion of the Sierra Castillo fault as an inherited and reactivated normal fault.

5. Seismic Interpretations of Subsurface Structures

5.1. Calama Basin

The structures under the Calama Basin have been interpreted from the EUCC91-04 seismic profile (Figure 10). This profile has a length of 26.7 km between the Río Loa Canyon and the westernmost slopes of the Cerros de Ayquina (Figure 3a). The central section of the profile is composed by a prominent package of sub-parallel, continuous, sub-horizontal, and high amplitude reflectors recognized between 0.7 and 2.5 s (two-way travel-time), which are correlated to the volcano-sedimentary syn-rift fill deposited between the Carboniferous-Permian and the early Upper Cretaceous (Collahuasi Fm., Tuina Fm., Caracoles Gr., and Tonel Fm., respectively; A. J. Tomlinson et al., 2018). To the east, these reflectors reach a greater thicknesses and are truncated by a west-dipping inverted normal fault. Both the seismic reflectors and the position of the fault may be defined as a half-graben basin. Upon contact with the fault, the top of the syn-rift sequences is folded and locally elevated over its regional

10.1029/2022TC007378

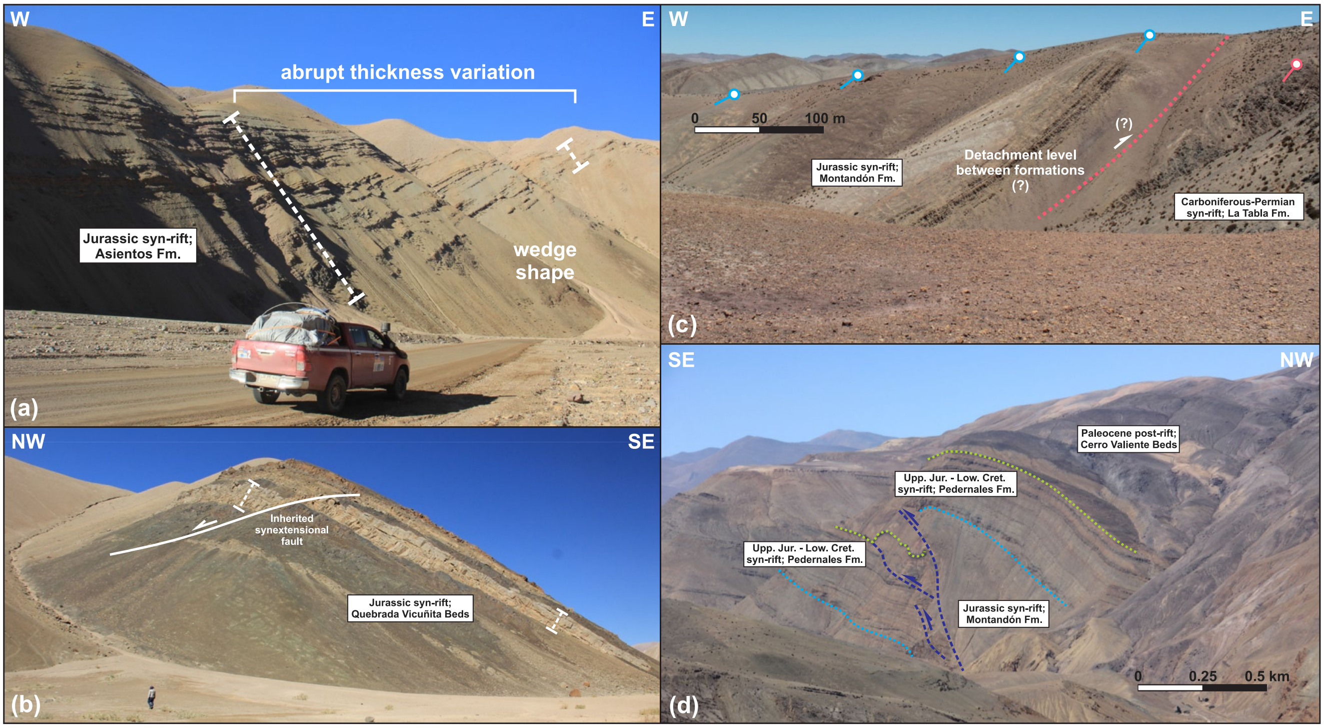

Figure 9. Some first-order structures exposed in the Potrerillos Fault and Thrust Belt. (a) Syn-rift wedge geometry involving Jurassic marine deposits. (b) Early normal fault. (c) Possible east-vergence thrust fault as a detachment level; the white segmented lines, in panels (a and b), highlight the beds thicknesses variations. (d) El Choclo fault as a "fault-bend fold," in which a hanging-wall anticline is exposed.

datum, thus evidencing a partial and positive reactivation of a previous normal fault (Figures 10c and 10d). To the east, a west-verging shortcut fault decapitates the main, partially inverted normal fault. The short-cut fault is generated from an east-dipping inverted normal fault related to a second half-graben structure; subsidiary normal faults control the syn-rift fill. Finally, the opposite-verging thrust faults affect both the Upper Cretaceous and Oligo-Miocene reflectors. To the west, a series of east-verging thrust faults affect the basement and the basin infill. Also, a minor intrusive body is emplaced along these structures.

5.2. Salar de Punta Negra Basin

To describe the structures buried below the southern Punta Negra Basin, we refer to the interpreted MX03 seismic profile (Figure 11). This cross-section reaches a length of 44.8 km and is located to the south of the Salar de Punta Negra Basin, between the Sierra de Varas and the western flank of the Western Cordillera (Figure 5a). Its interpretation allowed us to identify two tectonic domains. The first domain consists of east-verging faults located under the eastern border of the Salar de Punta Negra Basin. The second domain consist of west-verging faults located to the eastern border to the Salar de Punta Negra Basin. Within the east-verging faulting domain, the main seismic feature consists of a package of parallel, continuous, horizontal, and high-amplitude reflectors identified between ca. 0.5 and 1.8 s (two-way travel-time). These reflectors are associated with the syn-rift sedimentary infill deposited between the Carboniferous-Permian and the Upper Jurassic (La Tabla, Sierra de Varas, Profeta formations, respectively). To the east, the syn-rift reflectors are truncated by a partially inverted west-dipping normal fault bounding a graben or half-graben basin. To the west of the seismic line, two east-verging thrust faults affect reflectors associated with the basement and syn-rift sequences. These thrust faults expose the Carboniferous-Permian and Triassic sequences along the eastern flank of the Domeyko Cordillera. Apparently, semi-continuous and medium-amplitude reflectors located within the basement could correspond to a decollement level, which propagates as thrust faults. Also, both east-verging thrust faults generated subsidiary-structure developed as "leading imbricate fan" thrust systems (*sensu* Boyer & Elliot, 1982); minor back-thrust faults departing from these same structures can also be recognized. In particular, within the west-verging faulting domain, the structures consist of a interaction between west-verging thrust faults decapitating a previous west-dipping

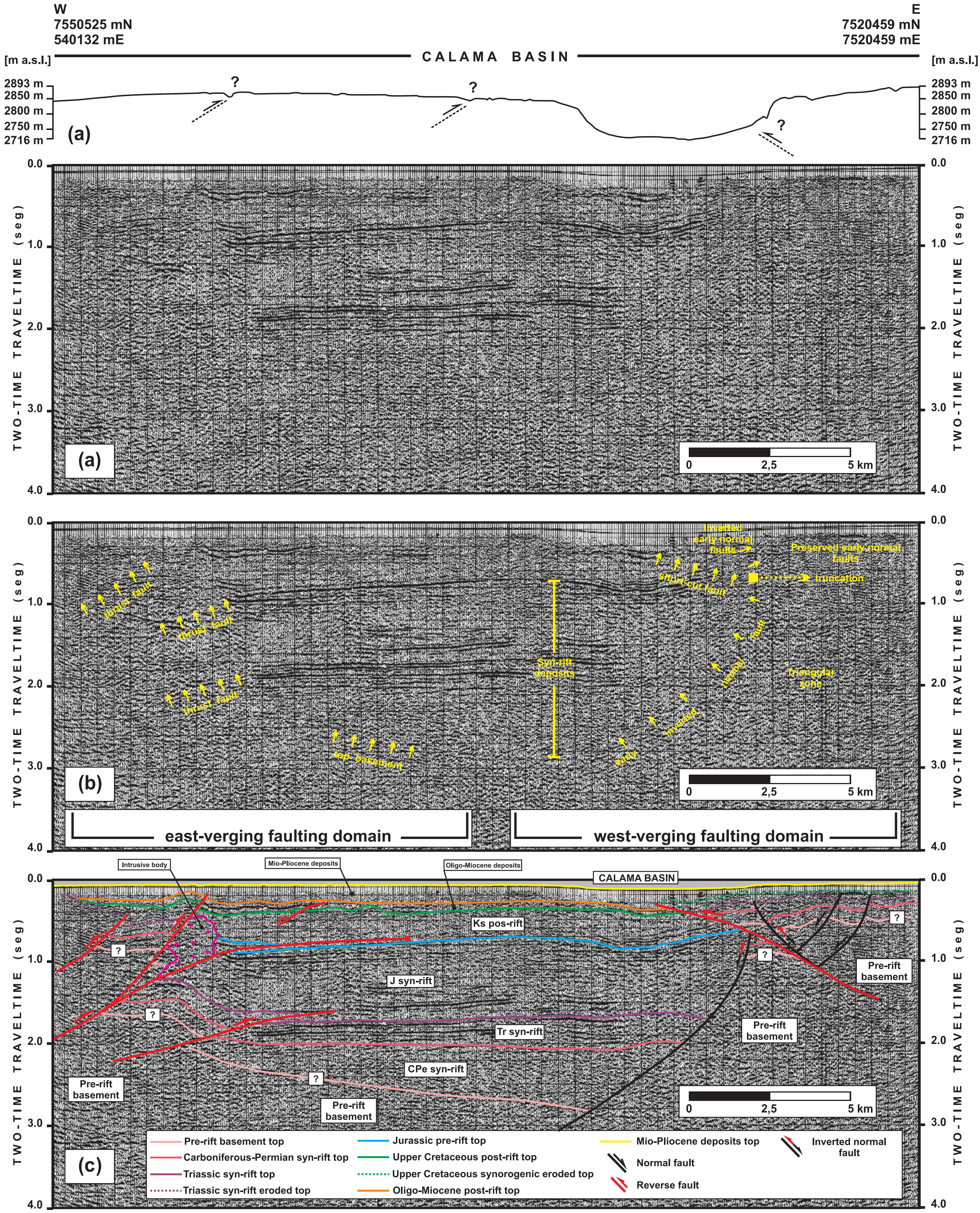

Figure 10. MX03 seismic line. (a) Uninterpreted gray-scale seismic line. (b) Interpreted gray-scale seismic line highlighting the characteristics interpreted from seismic reflectors. (c) Interpreted gray-scale seismic line showing the tectonosequences and the main structures. See Figure 3 for location.

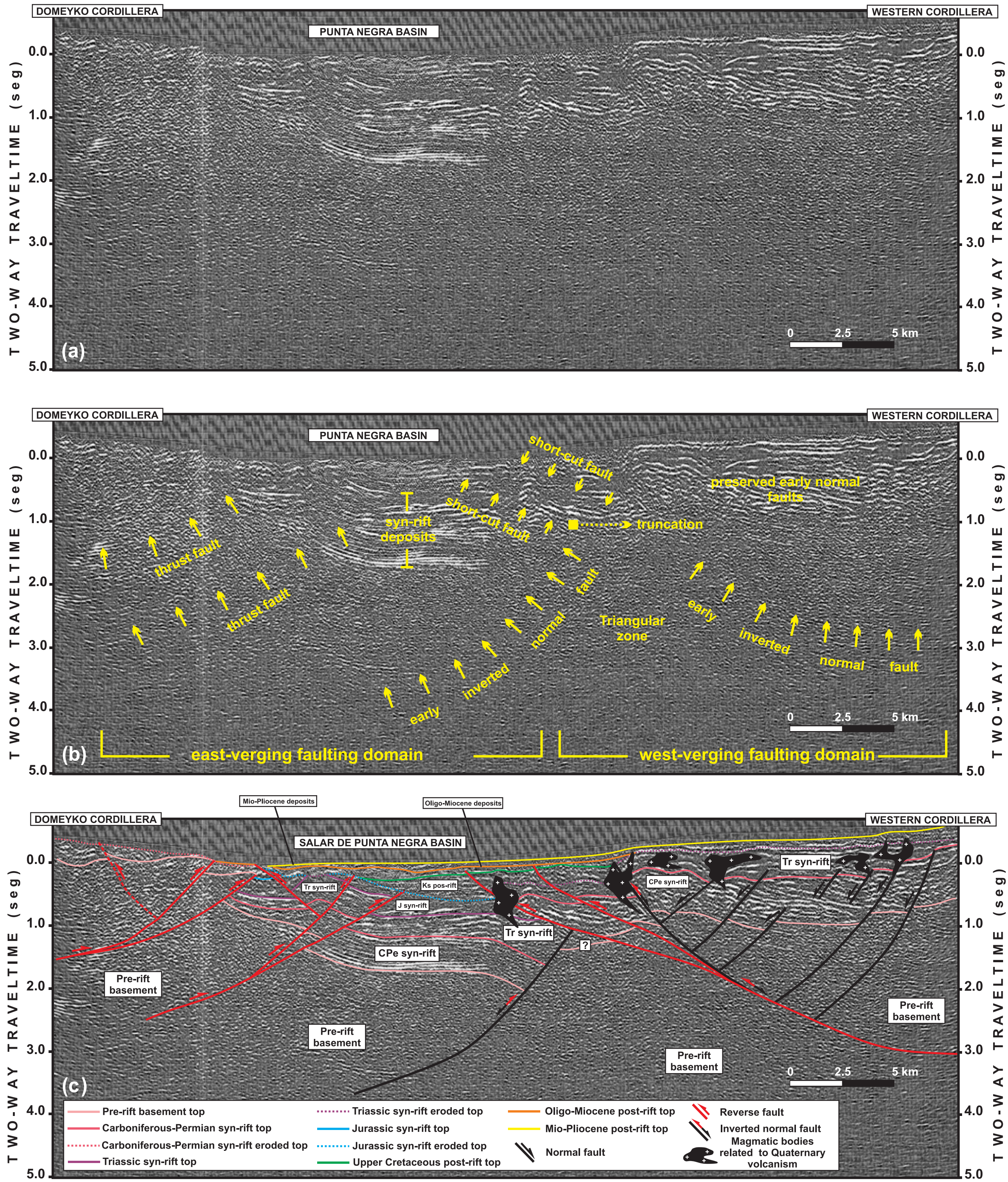

Figure 11. EUCC91-04 seismic line. (a) Uninterpreted gray-scale seismic line. (b) Interpreted gray-scale seismic line highlighting the characteristics obtained from seismic reflectors. (c) Interpreted gray-scale seismic line showing the tectonosequences and the main structures. See Figure 5 for location.

inverted normal fault. More specifically, the thrust faults correspond to shortcut faults, which formed as inversion structures from a partially east-dipping inverted normal fault controlling the Carboniferous-Permian and Triassic syn-rift deposits. Early minor and antithetic normal faults are recognized affecting the syn-rift fill of the half-graben basin.

5.3. Salar de Pedernales Basin

To describe the structures under the Pedernales Basin, we refer to our description of the PD-03 seismic line, which has also been complemented with the interpretations of the parallel PD-02 and PD-04 seismic lines proposed by Martínez, Kania, et al. (2020) (Figure 12). This profile reaches a length of 36.9 km, and it is located in the middle section of the Salar de Pedernales Basin, between the easternmost edge of the Potrerillos Fold and Thrust Belt and the western slope of the Claudio Gay Cordillera (Figure 8a). The main features consist of packages of parallel, continuous, horizontal, and high to medium-amplitude reflectors recognized between *ca.* 1.0 and 2.0 s (two-way travel-time). This feature can be attributed to the Upper Jurassic syn-rift sedimentary fill. Below these reflectors, a series of subparallel and diffuse reflectors would represent the earliest stages of syn-rift basin fill (Carboniferous-Permian to Triassic syn-rift deposits). In the central section, all these syn-rift reflectors are truncated by an east-dipping partially inverted normal fault related to the development of a half-graben basin. Other west-verging tectonic inversion-related structures can be recognized, such as, a footwall shortcut thrust and a hangingwall by-pass thrust that stand out to each side of this inverted normal fault. To the west of the seismic line, east-verging thrust faults affect the syn-rift reflectors. Finally, a prominent structure consists of an east-verging thrust fault, which decapitates an inverted normal fault, from a ramp recognized between ca. 3.0 and 5.0 s (two-way travel-time). Both east-verging thrust faults and east-dipping inverted normal faults are correlated with the faults previously recognized by Martínez, Kania, et al. (2020) from two seismic sections parallel to the PD-03 presented in this study.

6. Analog Modeling

A total of seven analog models are presented in this study (see Table 1 for details on modeling parameters). Two of them were developed exclusively under extensional conditions, thus establishing the initial setup of all the other models. The other five models were deformed through two superimposed deformational phases, a first extensional phase and a following shortening phase (positive inversion). Specifically, four models reproduced syn-rift sedimentation, and three were deformed under syn-shortening sedimentation.

6.1. Models ATM_01 and ATM_02: Initial Extensional Models, Without and With Syn-Rift Sedimentation

Model ATM_01 (Figures 13a and 13b) experienced only extension without syn-rift sedimentation (Table 1). In the final cross-section (Figure 13b), the main structures consist of two graben-type basins bounded by opposite-dipping normal faults. A horst stands out as a central block between both basins, which presents a 10° counterclockwise rotation around a horizontal axis. The dip of normal faults reaches an angle of approximately 70°. Antithetic and synthetic fault systems accommodate much of the subsidence within the graben basins. In plan view (Figure 13a), these faults limit and control a series of internal sub-basins housed within the main graben basins. However, the greatest subsidence is controlled by listric faults departing from the ductile silicone layer (PDMS). Minor features correspond to antithetic reverse faults and are subordinate to the main normal faults.

Model ATM_02 (Figures 13c and 13d) experienced extension coupled with syn-rift sedimentation (Table 1). In the final cross-section (Figure 13d), the main structures correspond to two graben basins bounded by a central horst, and the development of two half-graben basins located toward each edge of a basal silicone layer. Similarly to Model ATM_01, the central horst stands out for its counterclockwise rotation. The dip of normal faults reaches a mean angle of approximately 70°, and occasionally, the lower segment of the listric fault attains an angle of 20°. Antithetic and synthetic fault systems accommodate much of the subsidence within the graben basins. As in the previous model, in plan view (Figure 13c), these faults limit and control a series of internal sub-basins located within the main graben basins, which are characterized by the development of hanging-wall synclines. However, the greatest subsidence is still controlled by the main listric faults. Interestingly, minor features correspond to

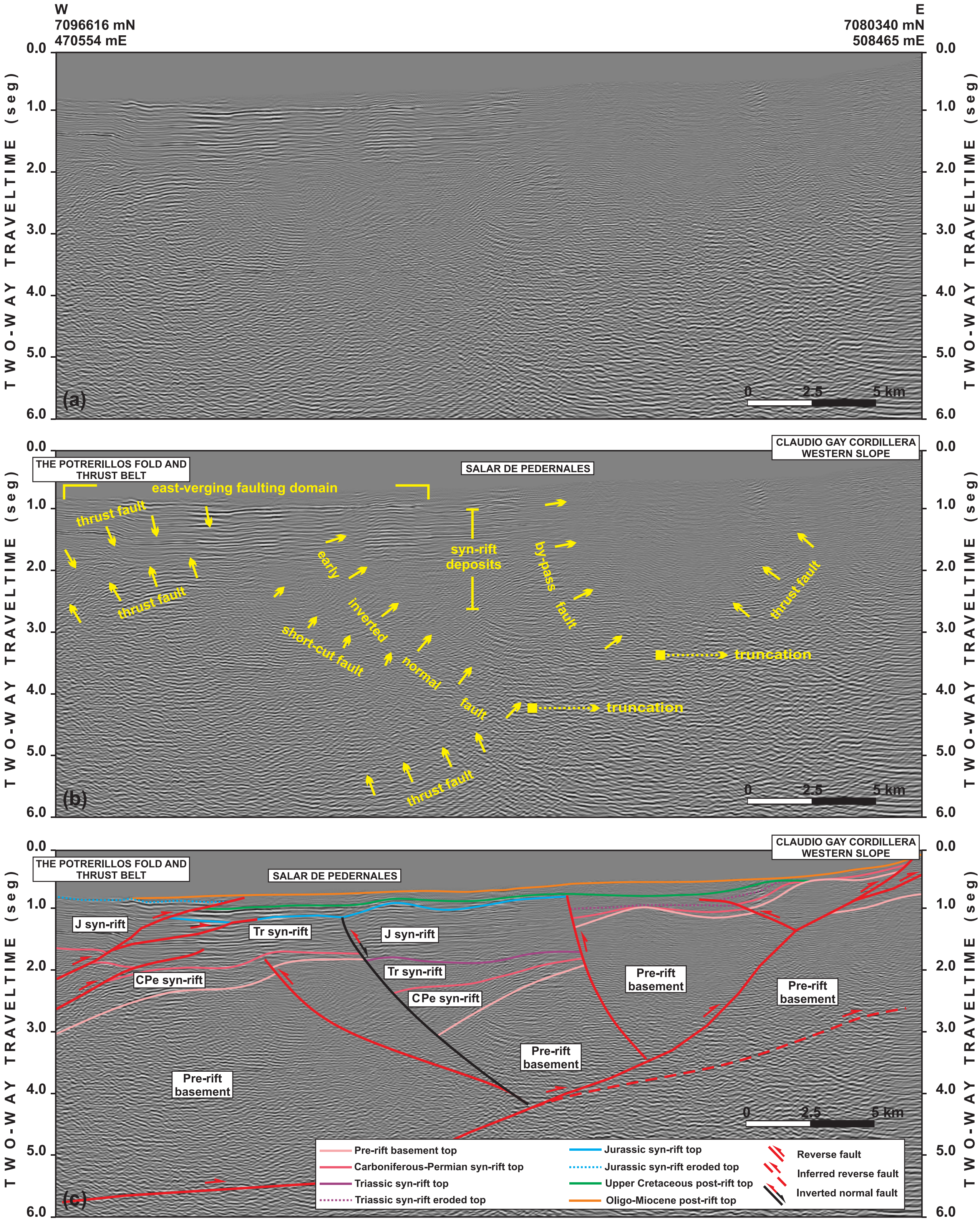

Figure 12. PD-03 seismic line. (a) Uninterpreted gray-scale seismic line. (b) Interpreted gray-scale seismic line highlighting the characteristics obtained from seismic reflectors. (c) Interpreted gray-scale seismic line showing the tectonosequences and the main structures. See Figure 8 for location.

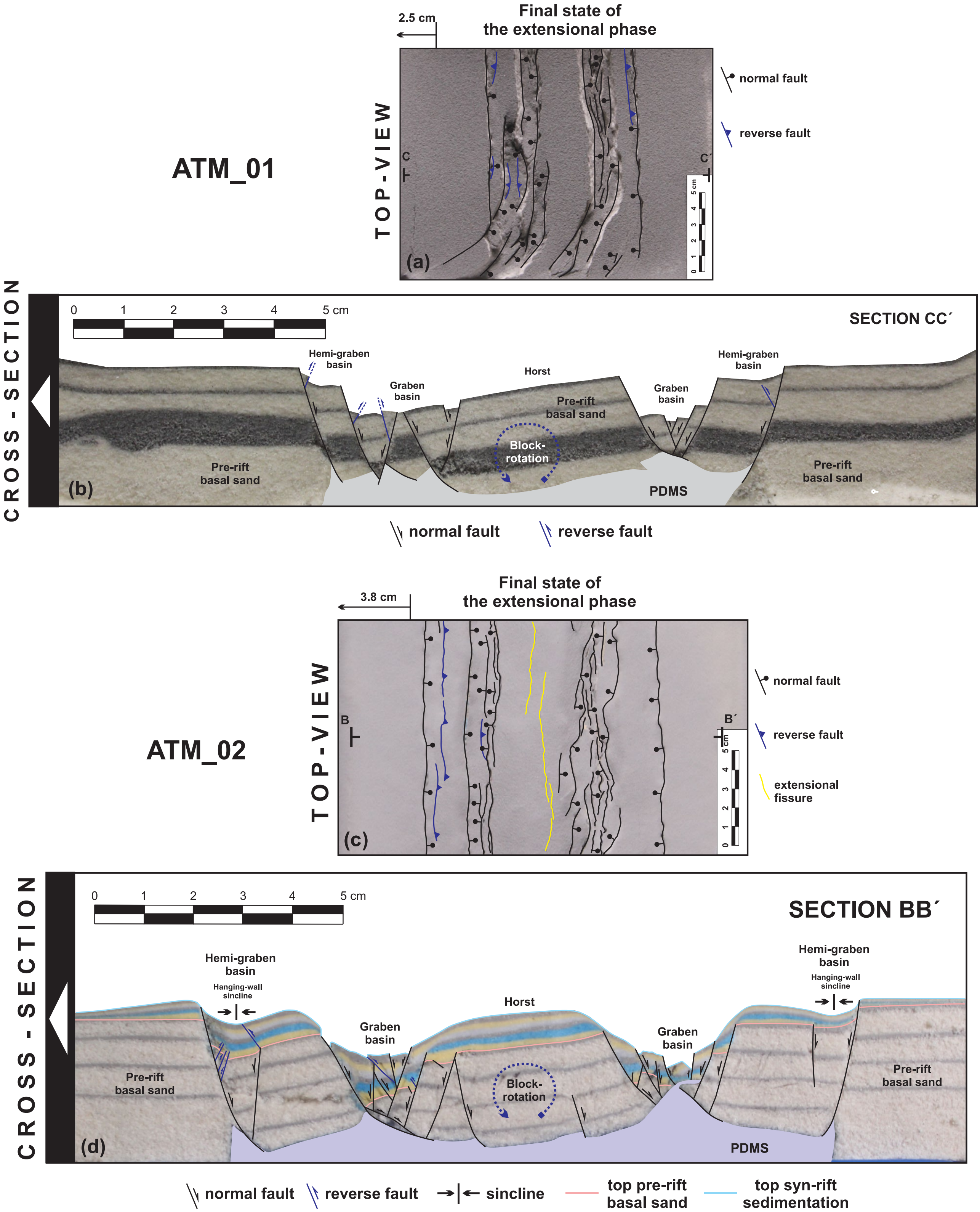

Figure 13. Model ATM_01 and Model ATM_02. Model ATM_01 corresponds to a pure extensional model. (a) The image shows the final state of the extensional phase in plan-view, respectively. (b) The image shows the final CC′ cross-section, interpreting the distribution of the normal faults. Note the reverse faults generated as antithetical faults to the main normal faults. Model ATM_02 corresponds to a pure extensional model with syn-rift sedimentation. (d) The images show the initial phase and final extensional phase in plan-view, respectively. (e) The image shows the final BB′ cross-section, interpreting the distribution of the normal faults. Note the reverse faults generated as antithetical faults to the main normal faults and a hanging-wall syncline affecting the syn-rift sedimentation.

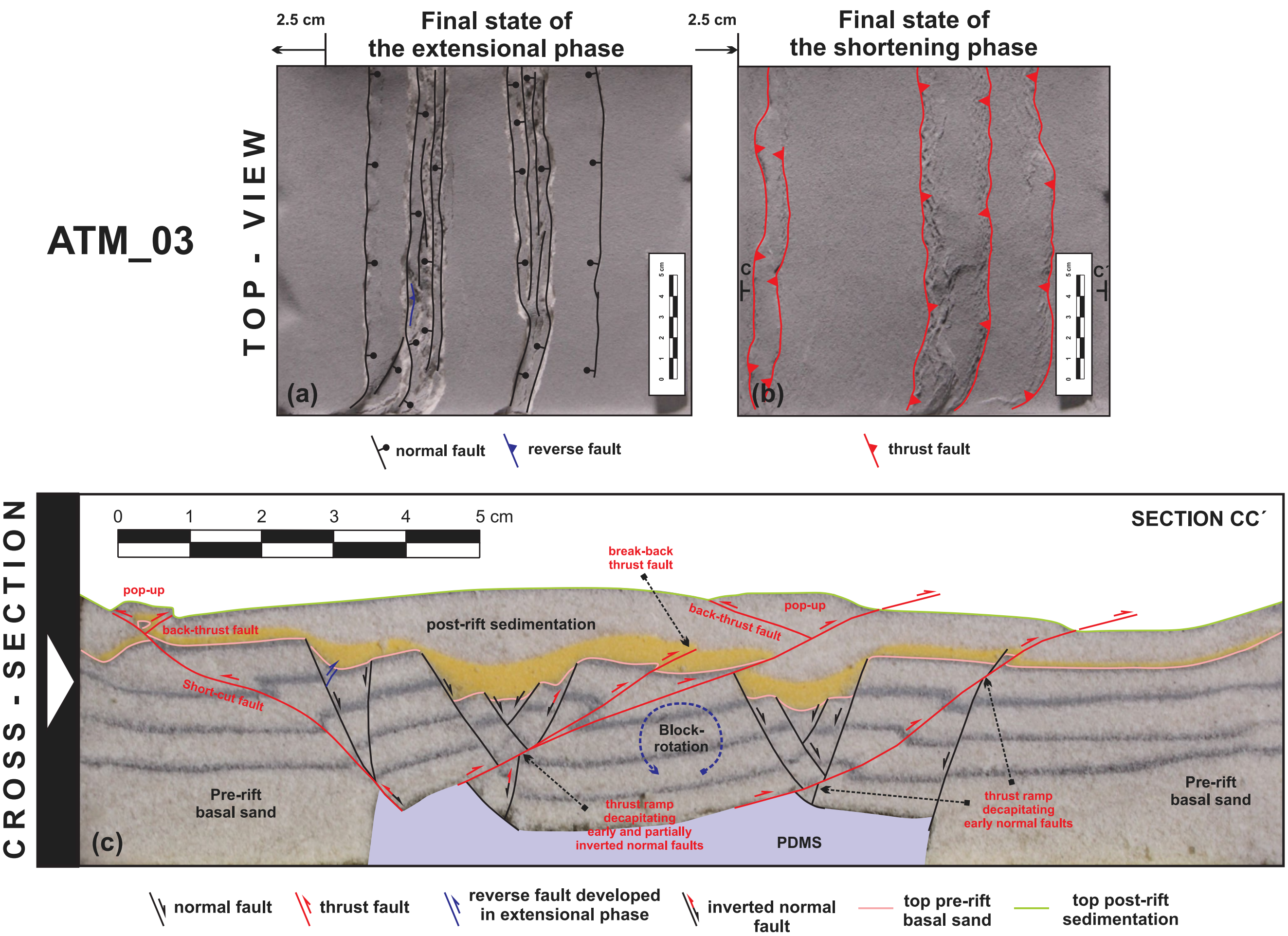

Figure 14. Model ATM_03. Model ATM_03 corresponds to an inversion model, without syn-rift sedimentation, and with a post-rift sedimentation phase. (a and b) The images show the final state of the extensional phase, and the final shortening phase, respectively, in plan-view. (c) The image shows the final CC′ cross-section, interpreting the distribution of the normal faults, inverted normal faults, and pure thrust faults.

a high-angle reverse fault accommodating the development of the hanging-wall syncline, as well as antithetic reverse faults also affecting the syn-rift sedimentation.

6.2. Model ATM_03: Positive Inversion Model Without Syn-Rift Sedimentation

Model ATM_03 (Figure 14) experienced inversion, coupled with post-rift sedimentation phases but without syn-rift sedimentation (Table 1). In the final cross-section (Figure 14c), normal faults are preserved after inversion; nevertheless, the main structures consist of three double-verging low-angle (from 15° to 25°) thrust faults, accommodating much of the shortening. One of these thrusts consists of a short-cut fault, which nucleated from the lower segment of a listric normal fault localized at the left of the cross-section and with an opposite vergence to the sense of shortening. The other two faults correspond to thrust ramps decapitating early normal faults. The latter two thrust structures have a same vergence with respect to the sense of shortening and their nucleation is controlled by the boundary between the ductile silicone layer (PDMS) and the pre-rift basal sand. In plain view, these structures generate the main topographic features (Figure 14b), affecting the model from the pre-rift basal sand to the post-rift sedimentation. Minor back-thrust faults only affect the post-rift coverage.

6.3. Model ATM_04: Positive Inversion Model With Syn-Rift Sedimentation

Model ATM_04 (Figure 15) investigated tectonic inversion accompanied by syn-rift sedimentation prior to the shortening (Table 1). In the final cross-section (Figure 15c), the main structures formed after inversion consist

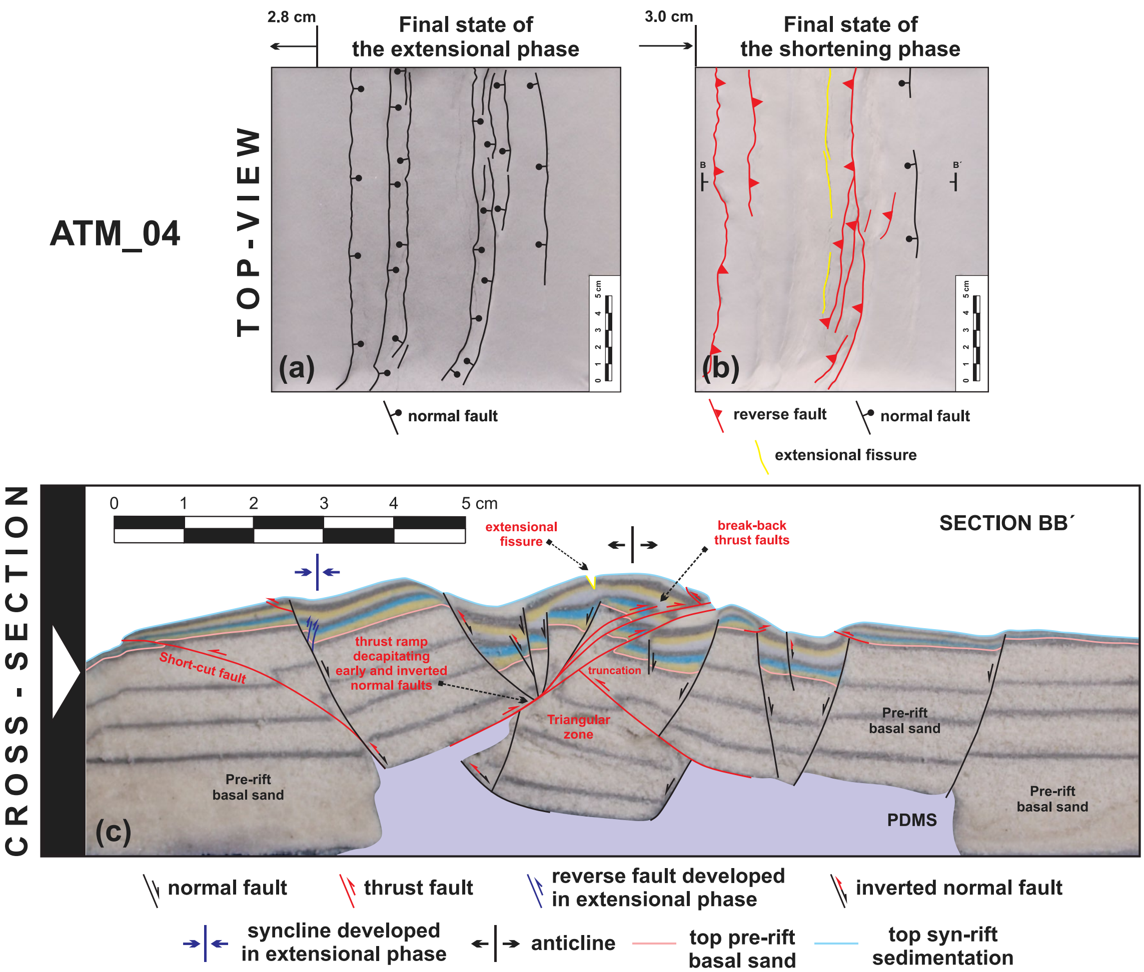

Figure 15. Model ATM_04. Model ATM_04 corresponds to an inversion model that only considers syn-rift sedimentation. (a and b) The images show the final state of the extensional phase and the final shortening phase, respectively, in plan-view. (c) The image shows the final BB′ cross-section of the inversion model, interpreting the distribution of the normal faults, inverted normal faults, and pure thrust faults. Note the pure thrust faulting (red lines), mainly as short-cut fault, break-back thrust sequence, and thrust ramp decapitating early and inverted normal faults.

of three thrust faults. The first one corresponds to a short-cut fault nucleating from the lower segment of a listric normal fault localized in the left part of the cross-section. This structure presents a convex shape with an average dip of 20° and with a vergence opposite to the direction of shortening. The second structure consists of a thrust system with an inclination of about 40° and vergence in the direction of shortening. This fault decapitates early and partially inverted normal faults, thus generating the major topographic feature, transporting the extensional depocenters (or graben basin) on the hanging-wall block. The third thrust fault has an average inclination of 40° and a vergence opposite to the sense of shortening. This structure decapitates the base of the normal faults that controlled the preserved extensional depocenters after the inversion (to the right of the cross-section, Figure 15c).

6.4. Models ATM_05 and ATM_06: Positive Inversion Models With Syn-Rift and Syn-Shortening Sedimentations

Model ATM_05 (Figures 16a–16c) experienced positive inversion and involved both syn-rift and syn-shortening sedimentations (Table 1). The deformation velocity was 25 mm/hr generating an approximate shortening of 2.7 cm. In the final cross-section (Figure 16c), the major structural feature corresponds to a graben basin filled by the syn-rift sediments, extruded, and transported over the hanging wall of the main thrust faults. The main structures are two low-angle thrust faults affecting both the pre-rift basal sand and the syn-rift sediments. The first, corresponds to a short-cut fault nucleating from the lower segment of a normal fault located at the left of the cross-section; its vergence is opposite to the main shortening sense. The second, represents a thrust fault which

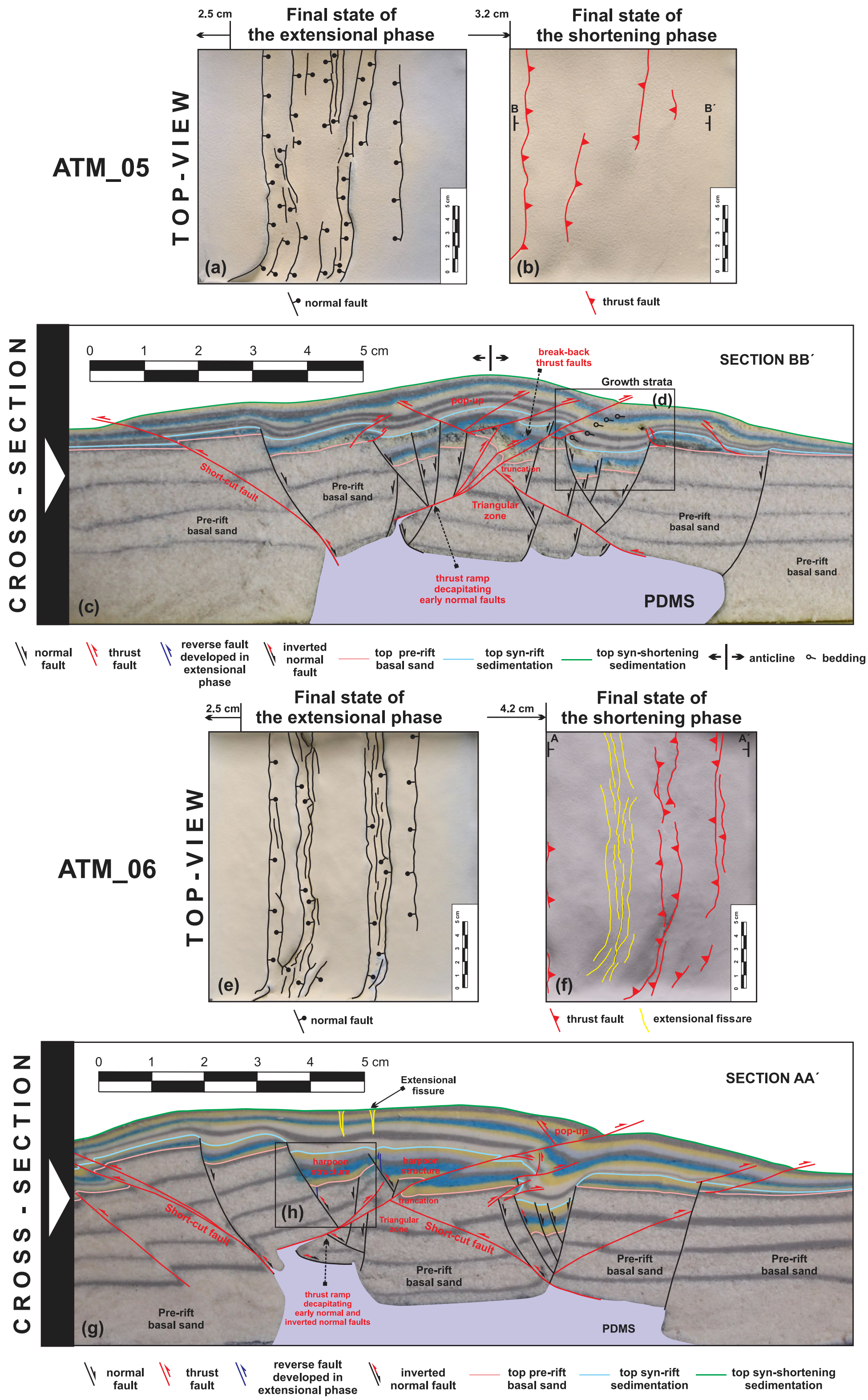
ATM_05
TOP-VIEW
2.5 cm
Final state of the extensional phase
3.2 cm
Final state of the shortening phase
(a)
(b)
B
B´
normal fault
thrust fault
CROSS - SECTION
0 1 2 3 4 5 cm
SECTION BB´
break-back thrust faults
Growth strata
(d)
pop-up
truncation
Short-cut fault
Pre-rift basal sand
Triangular zone
thrust ramp decapitating early normal faults
PDMS
(c)
normal fault
thrust fault
reverse fault developed in extensional phase
inverted normal fault
top pre-rift basal sand
top syn-rift sedimentation
top syn-shortening sedimentation
anticline
bedding
ATM_06
2.5 cm
4.2 cm
(e)
(f)
A
A´
extensional fissure
Extensional fissure
SECTION AA´
harpoon structure
(h)
Triangular zone
thrust ramp decapitating early normal and inverted normal faults
(g)

Figure 16.

generates the greatest displacement and the greatest topographic expression. This fault causes the decapitation and the transportation of early normal faults. A minor third thrust fault is truncated by the main thrust fault, generating a triangular zone. The latter thrust fault has an opposite-vergence to the main shortening sense and decapitates early normal faults. Minor double-verging thrust faults affect the syn-rift sedimentation and syn-shortening sediments reaching the model surface (Figure 16c). Apparently, these faults are generated at the contact between the syn-rift sediments and the pre-rift basal sand, and correspond to a back-thrust fault with an associated pop-up structure. Finally, growth strata-related geometry in the syn-shortening sediments is recognized. This geometry is located in the footwall of the thrust fault and is characterized by the variation in the dip of the syn-shortening sedimentation.

Model ATM_06 (Figures 16e–16g) corresponds to an inversion model that incorporated syn-rift and syn-shortening sedimentations. Unlike the model ATM_05, in Model ATM_06, the deformation velocity was 50 mm/hr generating an approximate shortening of 4.0 cm (Table 1). In the final cross-section (Figure 16g), the main structures are inherited normal faults, partially inverted normal faults, and double-verging thrust faults. The thrust faults consist of short-cut faults and a thrust fault with dip ranging from 25° to 45° affecting the pre-rift, syn-rift, and syn-shortening model sediments. The short-cut faults nucleate from the lower segment of border-normal faults in the left side of the graben basin and exhibit opposite vergence to the main shortening sense. The thrust fault accommodates most of the shortening and decapitate both early normal faults and partially inverted normal faults. This deformational process induces transport and uplift of the graben basin and the syn-rift sedimentary fill over the hanging-wall of the thrust fault. The vergence of this thrust fault is concordant to the shortening sense. Its inclination varies with depth, being 25° in the pre-rift segment, and decreasing to 15° in the syn-rift-syn-shortening segment. Another important minor feature are partially inverted faults, which cause inversion anticlines (or harpoon structures) involving the syn-rift sediment (Figure 16g).

6.5. Model ATM_07: A Positive Inversion Model With Syn-Rift, Post-Rift, and Syn-Shortening Sedimentations

Model ATM_07 (Figure 17) is another inversion model that incorporated syn-rift sedimentation, post-rift sedimentation, as well as syn-shortening sedimentation (Table 1). In the final cross-section (Figure 17c), the main structures consist of inherited normal faults, partially inverted normal faults, and double-verging thrust faults. Two parallel-thrust faults generated the greatest shortening and the greatest topographic expression. In general, all compressional structures dip between 35° and 30°. These thrust structures correspond to a thrust ramp decapitating early normal faults generating a prominent pop-up structure, affecting both the pre-rift basal sand and the syn-shortening sediment. Also, short-cut faults were generated from the border-normal faults that control the main graben basins. Similarly to the previous models, the thrust fault caused transport and exhumation of the graben basin and the syn-rift sedimentary fill, on the hanging wall of the thrust fault. Other inverted structures are restricted to some partially inverted normal faults. Among these, a structure related to positive inversion of the syn-rift sedimentary fill corresponds to a "harpoon structure" (*sensu* McClay & Buchanan, 1992), generating the folding (anticline structure) of the syn-rift sedimentation (Figure 17d).

7. Discussions

7.1. Structural Style Controls: Insights From Analog Models

Geometries and kinematics of the structures obtained from our laboratory experiments are dependent on the kind of sedimentation and the relationship between velocity and the amount of shortening applied. The interplay of

Figure 16. Model ATM_05 and Model ATM_06. Model ATM_05 consists of a positive inversion model, involving both, the syn-rift sedimentation and syn-shortening sedimentation. (a and b) The images show the final state of the extensional phase, and the final shortening phase, respectively, in plan-view. (c) The image shows the final BB′ cross-section of the inversion model, interpreting the distribution of the normal faults, inverted normal faults, and pure thrust faults. Note the pure thrust faulting (red lines), mainly as short-cut fault, break back thrust faults by the change in transport direction, thrust ramp decapitating early and inverted normal faults, and normal fault localizing thrust-ramp. (d) The black box highlights a depositional geometry related to growth strata. Model ATM_06 corresponds to an inversion model, which incorporates syn-rift and syn-shortening sedimentations. (e and f) The images show the final state of the extensional phase, and the final shortening phase, respectively, in plan-view. (g) The image shows the final AA′ cross-section of the inversion model, interpreting the distribution of the normal faults, inverted normal faults, and pure thrust faults. Note the pure thrust faulting (red lines), mainly as short-cut faults, thrust ramp decapitating early and inverted normal faults, and partially inverted faults, causing (h) inversion anticlines (or harpoon structure) involving the syn-rift sedimentations.

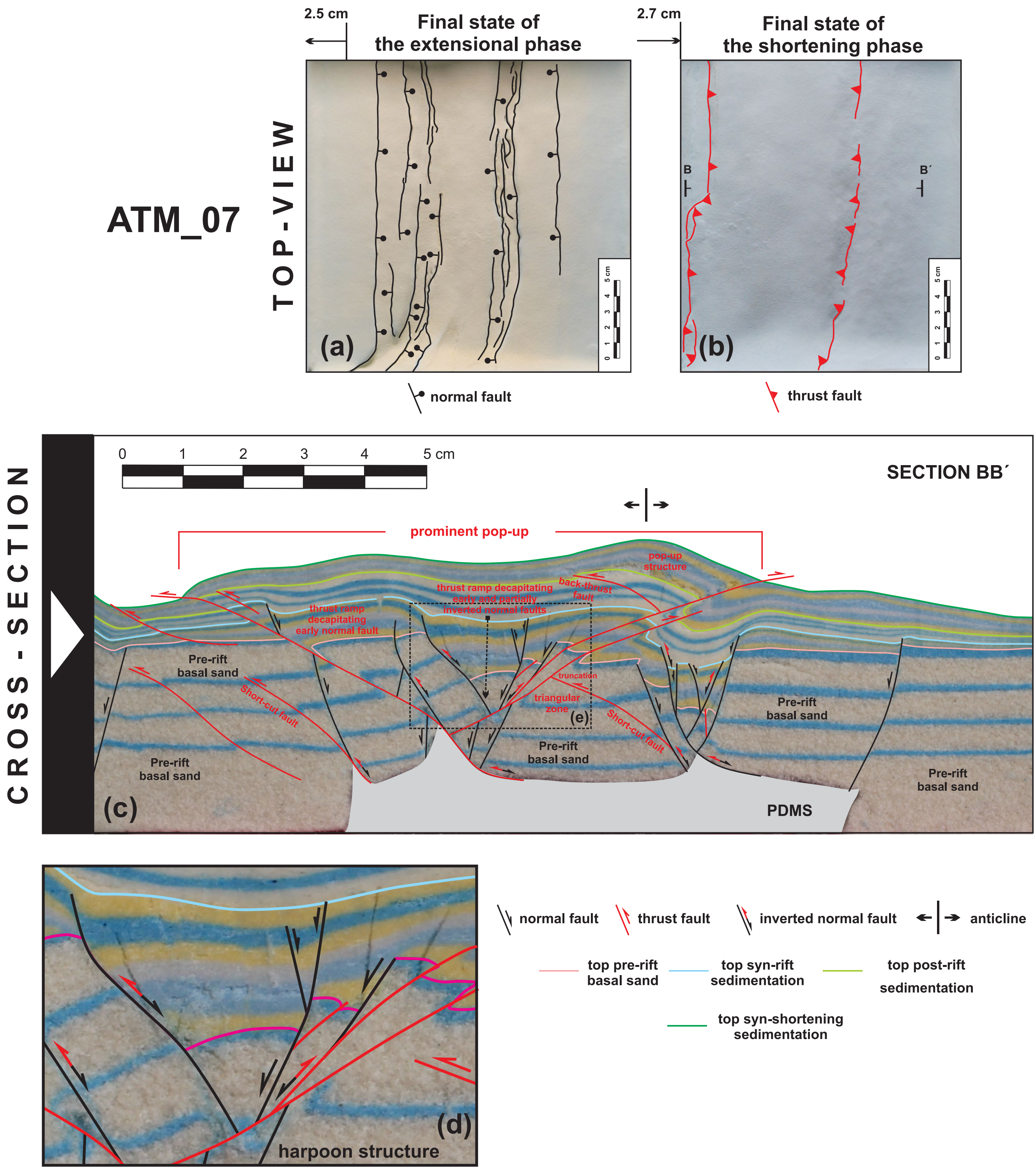

Figure 17. Model ATM_07. Model ATM_07 corresponds to an inversion model, which incorporates syn-rift sedimentation, post-rift sedimentation, and syn-shortening sedimentation. (a and b) The images show the final state of the extensional phase, and the final shortening phase, respectively, in plan-view. (c) The image shows the final cross-section of the inversion model, interpreting the distribution of the normal faults, inverted normal faults, and pure thrust faults. Note the pure thrust faulting (red lines), mainly as short-cut faults, thrust ramp decapitating early and inverted normal faults, and partially inverted faults, causing (e) inversion anticlines (or harpoon structure) involving the syn-rift sedimentation.

the structures formed during the extensional and shortening phases result in structural styles that may be homologated to natural cases such as those proposed in this study.

7.1.1. Structural Styles Developed During the Initial Extensional Phase

The distribution of high-angle faults and listric normal faults during the initial extensional phase is controlled by the rheological difference between the basal silicone layer (PDMS) and the pre-rift basal sand. This ductile/brittle interface is a favorable horizon for the nucleation of extensional structures and represents the basal detachment level. Thus, normal faulting may be compared to a typical model of cortical extension proposed by Parson and Thompson (1993), in which the formation of listric normal faults is induced by rheological changes. In this way, the position of the ductile silicone layer conditions the development of normal faults, and in turn, the formation of graben or half-graben basins. Specifically, two graben basins separated by central block-horst represented a common outcome (see Models ATM_01 and ATM_02; Figure 13). This structural pattern, together with the associated normal faults, will become part of inherited structures, some of which will be partially inverted during the shortening phase. Other subsidiary structures during the extensional phase are hanging-wall synclines and some reverse faults (see Model ATM_04; Figure 15). Generally, these structures form as secondary accommodation structures of the main high-angle normal fault, or specifically, from the master normal faults that bound the graben or half-graben basins (Imber et al., 2003; Xiao & Suppe, 1992).

7.1.2. Structural Styles Developed During the Shortening Phase

The structural styles developed during the shortening phase are dependent both the syn-rift sedimentation as well as the syn-shortening sedimentation. On the one hand, incorporation of the syn-rift sedimentation affects the pattern and the kind of structure that may develop during the shortening phase. Specially, Models ATM_03 and ATM_04 (Figures 14 and 15) present differences in kind, distribution, and number of structures developed during the shortening phase. This may be due to the load generated by the syn-rift sedimentation (incorporated in the model ATM_04). For example, the syn-rift fill could be a controlling part of the positive tectonic inversion, accommodating some of the initial shortening induced by reactivated early normal faults. Also, the syn-rift accumulation tends to form break-back thrusts-like structures, thus generating a greater topographic expression. On the other hand, the shortening phase is strongly dependent of the syn-shortening sedimentation (incorporated in the models ATM_05, ATM_06, and ATM_07). This accumulation conditions the formation of double-verging thrust faults from inverted faults or as back-thrust faults. These structures could be explained by a displacement transferred from deeper faults to superficial levels. Furthermore, faults affecting the pre-rift basal sand would vertically transfer deformation toward the syn-shortening sedimentation inducing a lateral and/or horizontal deformation (Medwedeff, 1990; Mount et al., 2011; Shaw et al., 2004). Compressional structures linked to the positive inversion consist of (a) short-cut faults, (b) partially inverted normal faults, (c) inversion anticlines, and (d) newly formed pure thrust faults. Usually, the short-cut faults (a) have an opposite-vergence to the shortening direction, and nucleate from the lower-dip segment of the normal faults located toward the left edge of each developed inversion model (Figures 14–17). The partially inverted normal faults (b) are the result of an inversion of the east-dipping normal faults (or to the right of the cross-section), which control graben structures. In turn, these basins expose inversion-related anticlines (c), showing an apparent arrowhead geometry or harpoon structure (Williams et al., 1989) (see Models ATM_06 and ATM_07) and with a wedge-shape that thickens toward the partially inverted right-dipping normal faults (Figures 16 and 17). Finally, newly formed pure thrusts (d) originate from a detachment level between the ductile silicone layer (PDMS) and the pre-rift basal sand. In the latter structures, (a) thrust ramps decapitate early or inverted normal faults, (b) break-back thrust faults, and (c) normal faults localizing thrust-ramps may be differentiated. Furthermore, some back-thrust faults may generate pop-up structures, mainly affecting the syn-shortening sediments. Both "thrust ramp decapitating early or inverted normal fault" and "break-back thrust faults" kinematically correspond to thrust systems, and thus generate the greatest shortening and the greatest topographic expression. Occasionally, these structures generate prominent pop-up structures (see Model ATM_07; Figure 17), affecting all the model thickness, from the pre-rift basal sand to the syn-shortening sediments. Therefore, four first-order structural styles are recognized as common and recurring deformational features after the shortening phase: (a) Early or inverted normal faults, (b) preserved graben basins transported as part of hanging wall (e.g., thrust ramp decapitating early inverted normal faults) and lifted by (c) newly formed thrust faults, which may uplift the pre-rift basal sand-blocks and the syn-rift fill to upper levels, and finally, (d) growth-strata geometry in the syn-shortening sedimentation generated into the footwall of the thrust fault (see Model ATM_05; Figure 16).

Regarding the effect of the shortening velocity, the highest velocity (50 mm/hr, see Model ATM_06) resulted in a comparatively lower number of newly formed thrust faults (only four opposite-verging thrust faults) with respect to models deformed at lower shortening velocity. Also, the development of folds during the syn-shortening sedimentation was small or almost absent; however, pure thrust faulting developed from a higher shortening velocity may have generated the largest exhumation of the pre-rift basement (Figure 16).

7.1.3. A Generalized Kinematic Model

By comparing and integrating our modeling results and the interpreted structural styles for each model, we propose a generalized kinematic model (Figure 18) considering an extensional phase, going through a positive tectonic inversion phase, to a final shortening phase. On the one hand, Figure 18a represents a generalized model developed in an initial extensional phase, which is characterized by widespread normal faulting and accompanied by accumulation of the syn-rift fill of graben and half-graben basins. Here, two kinds of normal faults stand out. To the right, the high-angle faults develop hanging wall synclines accommodating the extensional faulting. To the left, the low-angle faults are characterized by a listric geometry. A series of antithetic and synthetic normal faults mainly accommodate the extension (or subsidence) within the graben basins. On the other hand, Figure 18b represents a generalized model developed from a positive tectonic inversion of the previous extensional phase. Here, two structures stand out: (a) early and partially inverted normal faults and their syn-rift geometry-related deposits, and (b) newly formed pure thrust faulting. The first structure corresponds to the partial inversion of previous normal faults and represents the initial phase of positive inversion and exhumation of the syn-rift deposits. The second structures represent pure thrust faults and consists mainly of low-angle double-verging thrust faults. The newly formed thrust faults generate the greatest shortening, the greatest exhumation, and decapitate early or partially inverted normal faults, transporting them along their hanging wall. Moreover, its flat-ramp-flat geometries generate a counter-clockwise rotation of the blocks, rotating the inclination of the early inverted normal faults. Pure thrust faulting represents the final phase of shortening. These structures transport and uplift the pre-rift basement and the syn-rift deposits as an inherited passive tectonic block. As the compressional regime continues, deformation propagates with a same-vergence to the shortening direction. However, opposite-verging short-cut faults are also recognized. These faults may be generated as an opposite response to the continuous shortening or due to a critical state of maximum shortening. Considering the top of the syn-rift deposits as a reference marker of deformation for each phase of the model (Figure 18c), thus, we propose two interpretations related to the inheritance of the structural features. After the shortening phase, (a) the maximum formed elevations are due to the uplift and the transport of the syn-rift fill (Graben basin 1 in Figure 18c) located to the left of the model, evidencing the inheritance of the extensional structures and the syn-rift accumulation. (b) Graben basin 2 is hidden below the main east-verging thrust fault, preserving the early and partially inverted normal faults (Figure 18c).

Similar models obtained from the analog models experiments have been proposed to understand basin inversion and the role of inherited extensional geometries in the generation of newly formed thrusts in some examples of typical orogens worldwide (Del Ventisette et al., 2005, 2006; Jara et al., 2017; Martínez & Cristallini, 2017; Sani et al., 2007; Zwaan et al., 2022; among others). For example, Bonini et al. (2012) suggest that newly formed thrust faults are the preferential structures developed after positive tectonic inversion. These structures are defined as "hangingwall breakthrough" faults, dipping oppositely to the inverted faults and similarly to the back-thrust faults accommodating hangingwall deformation above thrust-ramp faults. Other studies (McClay et al., 2000; Munteanu et al., 2014) ratify that the pre-existing extensional domain is strongly influenced by the geometrical distribution of weak rheological inheritance, where deformation concentrates as active indenters that impose different thrusting vergences along the strike of the system.

7.2. Comparison of Models With the Structures Identified in the Domeyko Cordillera

The aim of performed analog models is to compare early normal faults, inversion structures, and pure thrust faulting with those structures recognized in the studied area by means of fieldwork and 2-D seismic profile interpretation. Specifically, to compare geometries and kinematics with structures that induced the orogenic growth of the Domeyko Cordillera, and even, to understand the initial uplift of the western flank of the Central Andes. The structural styles and distribution of faults that controlled the Domeyko Cordillera were strongly dependent on the inherited structures and pure thrust faulting (see Sections 4 and 5). For example, early basement normal faults were reactivated as high-angle reverse faults, thus generating regional-scale inversion anticlines and expelled

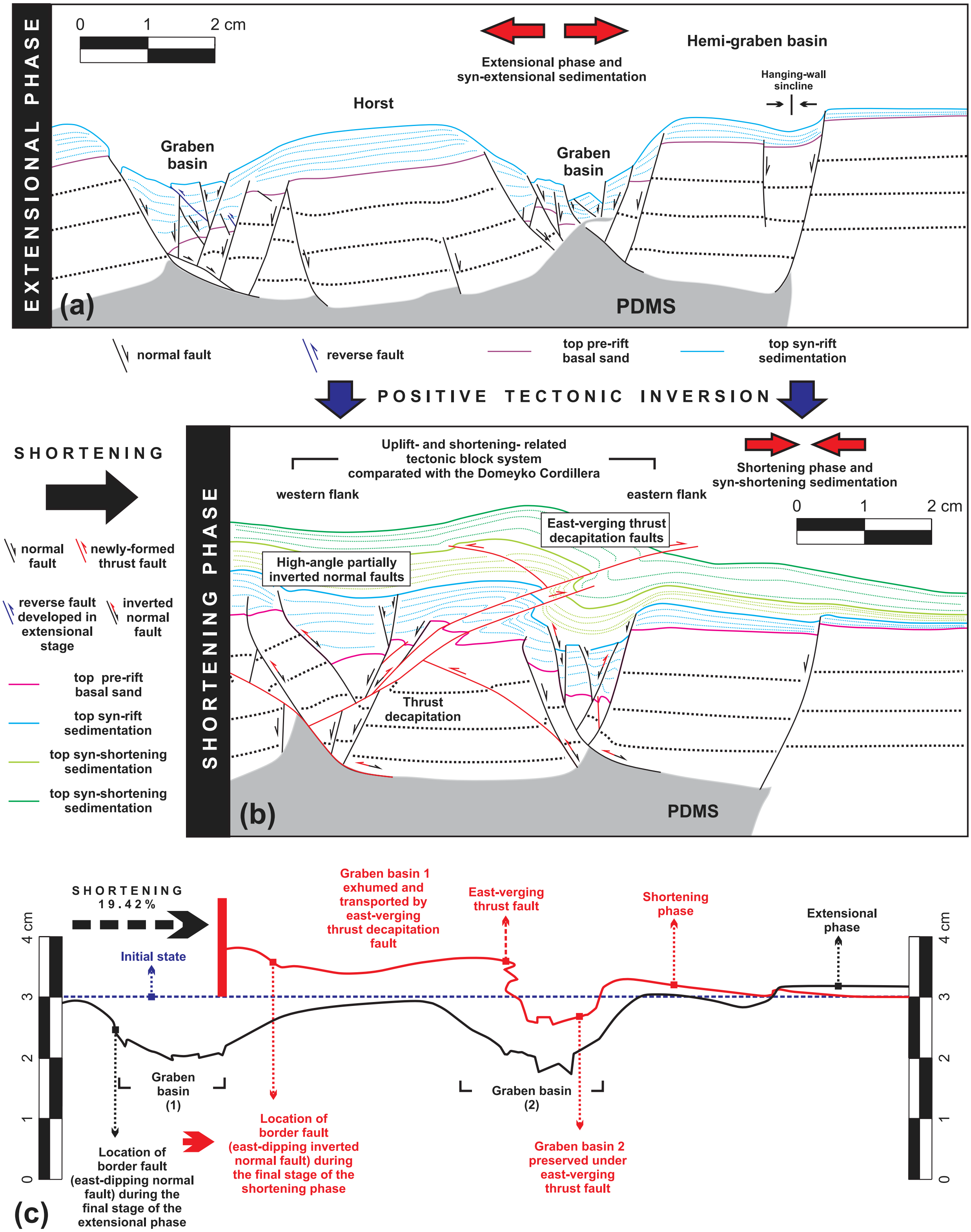

Figure 18. Generalized model for the two deformational phases. The model compares and integrates the results described and the structural styles interpreted and the main indicator of deformation for each analog model performed. (a) The figure represents a generalized model developed in an initial extensional phase with syn-rift sedimentation. (b) The figure represents a generalized model developed in a shortening phase from a positive tectonic inversion, involving all types of sedimentations. (c) The scheme considers the top of the syn-rift deposits as a referential marker of deformation, for each phase of deformation as a generalized model, highlighting the main interpretations related to the inheritance of the structural features.

syn-rift sequences from the half-graben structures. Furthermore, some inverted structures transferred the deformation to the late Cretaceous-Cenozoic synorogenic cover. In some locations, the high-angle partially inverted faults were decapitated and transported on hanging walls of thrust faults.

7.2.1. Structures Exposed on the Western Flank of the Domeyko Cordillera

A first comparison is associated with early inverted normal faults and the geometry of the syn-rift deposits (see the proposed model in Figure 18a), linked to extruded Mesozoic extensional basin fills and their associated structures. In particular, these structures show deformational features, such as west-verging inverted or partially inverted normal faults, inversion anticlines, and buttressing structures, among others. Notable examples are exposed on the western flank of the Domeyko Cordillera: specifically, to the west of the Calama Basin, to the west of the Salar de Punta Negra Basin, and the west of the Potrerillos Fold and Thrust Belt (see Section 4).

In addition, on the western flank of the Domeyko Cordillera, some of these high-angle master normal faults, defined as part of the Domeyko Fault System, have been previously interpreted as the product of strike-slip faulting (e.g., West Fault, Sierra de Varas Fault, and Sierra Castillo faults; see Figures 3, 6 and 10, respectively). Within this system, faults put Paleozoic basement rocks in contact with Mesozoic and Cenozoic sequences, and thus, it is questionable that essentially strike-slip structures may bring geological units of such dissimilar ages into contact and explain the orogenic growth, especially during the Upper Cenozoic. Rather, the relationships between this kind of faulting and its syn-rift deposits would respond to an inversion mechanism and subsequent extrusion of half-graben basins. When comparing the structural styles resulting from the analog models with the geometry of faults exposed on the western flank of the Domeyko Cordillera, the Domeyko Fault System may be redefined as the ancient border fault system of those rift basins active during the Carboniferous-Permian to Lower Cretaceous (Espinoza et al., 2018; López et al., 2020; Martínez, López, & Parra, 2020). In this interpretation, early east-dipping normal faults, associated with rifting, and west-verging inverted normal faults induced by the positive tectonic inversion of the rift basins have been preserved as structural limits of ancient tectonic blocks. These structures accommodated and controlled the initial stages of tectonic shortening and therefore, the initial orogenic growth of the Domeyko Cordillera. Normally, on the western flank of the Domeyko Cordillera, the folded Jurassic syn-rift successions are truncated by east-dipping inverted normal faults that could have resulted from the partial inversion of the Jurassic rift basins. These structures were reported by López et al. (2019) from a seismic profile interpretation which recognized partially inverted faults, immediately to the west of this study area. Similar interpretations along this segment were proposed by Amilibia et al. (2008) and Espinoza et al. (2021). These authors concluded that the Paleozoic and Mesozoic extensional faults exerted a marked control over the structural style in the orogenic growth of the Domeyko Cordillera. Therefore, an important control of a west-dipping inverted normal fault was proposed for the development of rift basin and its subsequent tectonic inversion (i.e., fault defined as the Grab Llano fault in Amilibia et al. (2008) and as the Profeta fault in Gonzalez et al. (2015), Espinoza et al. (2021), and this study).

This deformation pattern is also consistent with the West Vergence Thrust System (Farías et al., 2005) observed on the western flank of the Altiplano in northern Chile and structures recognized to the east of the Pampa del Tamarugal (Fuentes et al., 2018; Martínez, Fuentes, et al., 2021). Examples of inverted structures, as first-order mechanisms that have determined the style of tectonic inversion during relevant phases of orogenic growth, may be recognized in other orogenic chains such as the Apennines (Bonini et al., 2012; Del Ventisette et al., 2021; Scisciani, 2009; Vezzani et al., 2010), the Neuquén Basin and Salta Rift from the Argentinian Andes (i.e., Calderon et al., 2017; Giambiagi et al., 2008; Kley et al., 2005; Mescua & Giambiagi, 2012; Perez et al., 2016), and the western Alps (Welbon & Butler, 1992), among others. Specifically, along the western margin South American, the tectonic inversion of the Mesozoic extensional basins played an important role during the initial stages of the uplift of the Central Andes.

Although, we have interpreted the structures exposed mainly on the western flank of the Domeyko Cordillera as the result of the partial inversion of early normal faults, and subsequently, decapitated and transported by the east-verging thrust faults, we do not rule out a role of strike-slip faulting (Mpodozis & Cornejo, 2012; Niemeyer & Urrutia, 2009; Reutter et al., 1991). The oblique plate convergence (Pardo-Casas & Molnar, 1987), the high-angle of these faults, and the lubrication caused by the emplacement of subvolcanic intrusives (Boric et al., 1990; Maksaev & Zentilli, 1988; Mpodozis & Cornejo, 2012; Mpodozis et al., 1993) played a fundamental role as strike-slip fault reactivations. However, the strike-slip faults are not the first-order structures associated with the relevant uplift events that led to mountain building of the Domeyko Cordillera.

7.2.2. Structures Exposed on the Eastern Flank of the Domeyko Cordillera

A second comparison is associated with the newly formed pure thrust faults (see the proposed model in Figure 18b). On the basis of the interpretations from the analog models, one of the main mechanisms for generating shortening and uplift is related to low-angle thrust faulting. Structures with such kinematic and geometric characteristics were recognized in our three proposed segments studied. Specifically, in the Domeyko Cordillera and the Pre-Andean Basins transitional zone, the seismic lines show east-verging thrust faults (see Figures 10–12), which constitute a first-order structural control and a marked structural boundary between these morpho-tectonic units. Here, low-angle thrust faults may decapitate inherited and partially inverted normal faults preserving syn-rift deposits under the late Cretaceous-Cenozoic synorogenic sequences that filled the Pre-Andean Basin. Similarly, to the westernmost section, west-verging thrust faults decapitate preserved extensional structures. This kind of structural style has been related to basins described as "doubly vergence inverted basins" which are characterized by non-extruded depocenters during positive tectonic inversion (Jara et al., 2017).

The term "thrust decapitation" was proposed for other orogens in the world to indicate the effects of variations of rift basin geometry on the development of thrust belts. These structures resulted from inherited rheological weakness, such as evaporitic stratigraphic levels, reservoirs of magmatic arcs, and previous inverted listric normal faults. The latter may be propagated as a short-cut fault (Pace et al., 2014) and thrust ramp decapitating an early or inverted normal fault (e.g., Coward et al., 1991; Scisciani, 2009; Tavarnelli, 1996). For example, in the French Alps (Welbon & Butler, 1992), the early normal faults were affected by the thrust, thus generating variations in early fault geometries, and forming thrust belts. The geometries of late thrust induced a wide variety of structural forms. Also, in the Apennine chain (Italy), Scisciani (2009) revealed that steeply E- and W-dipping Mesozoic-Cenozoic normal faults are systematically decapitated by sub-horizontal or gently west-dipping thrusts propagating with short-cut trajectories. Also, in the Apennine chain (Italy), Del Ventisette et al. (2021) proposed an interaction between the Quaternary faults and the pre-existing low-dipping thrusting faults.

7.2.3. The Relationship Between Inverted Normal Faults and Pure Thrusting

If we consider the interpretations of analog models and the seismic lines, the east-verging thrust systems proposed here could be also considered as "a long-scale thrust decapitation system." Such thrust decapitation would also affect the high-angle inverted normal faults exposed on the western flank of the Domeyko Cordillera. In this way, the structures exposed on the western flank of the Domeyko Cordillera register, particularly, three structural styles related to their kinematic nature: (a) normal faulting generated during the extensional regime from the Permo-Triassic to the Lower Cretaceous. (b) Inversion or partial inversion of these normal faults during the Upper Cretaceous positive tectonic inversion, associated with the late Cretaceous Peruvian Tectonic Phase, which generated high-angle and west-verging inverted normal faults. (c) Decapitation and transport of such inverted faults on the hanging-wall of east-verging thrust faults, as a consequence to continuous shortening, possibility related to the Eocene-Oligocene Incaic Tectonic Phase. This mechanism would control the exhumation of Paleozoic basement blocks, such as those exposed in the Sierra de Limón Verde and the Sierra de Castillo. On the eastern flank of the Domeyko Cordillera, the east-verging thrust decapitation faults would form a geometry of fault-bend folds defined by ramps-planes-ramps. In the same way, half-graben basins were hidden under the late Cretaceous-Cenozoic synorogenic coverage that filled the Pre-Andean Basins. Thus, the greatest shortening and the greatest topographic features throughout the entire Andean forearc may be related to this deformation mechanism, playing a fundamental role in the uplift of the Domeyko Cordillera and the formation of the Pre-Andean Basins. For this thrust system, we suggest a detachment level associated with the rheological boundary between the brittle crust and the ductile crust at a depth of approximately 20 km (Bloch et al., 2014). If it is assumed that, after the Peruvian Tectonic Phase, the forearc underwent a thermal episode related to the emplacement of igneous bodies, these would have constituted a favorable detachment level controlling the thrusting in the upper crust. At the latitude of the Calama Basin, this nucleation or detachment level may be correlated with the Calama Bright Spot reflector analyzed in the PRECORP regional seismic profile that runs E-W (Yoon et al., 2003, 2009).

8. Concluding Remarks

The architecture and geometry of structures that control the orogenic growth of the Domeyko Cordillera is the result of a long-term complex history of superimposed tectonic events. However, the relationships, areal distribution, and kinematic nature of structures are barely known and difficult to understand. Based on analog models, seismic line interpretations, and new structural field data presented in this study, we present new results and new ideas that may help to improve the understanding of the Domeyko Cordillera and may also offer new knowledge about the evolution of the Andean forearc of the Central Andes. Our most relevant results are summarized as follows:

1. The Domeyko Cordillera is interpreted as an uplift- and shortening-related tectonic block system, which has interacting west-verging high-angle inverted normal faults and east-verging thrust decapitation faults. Our analog models geometrically replicated the distribution and the kinematics of exposed structures on each flank of the Domeyko Cordillera, thus suggesting that mountain building was induced, in its initial stage, by positive tectonic inversion of the rift basins. Furthermore, newly formed pure thrusts are the dominating structures during orogenic development after tectonic inversion.
2. Our analog models replicated extensional conditions, which are preserved after tectonic inversion. Based on seismic line interpretation and fieldwork data, this kind of extensional inheritance is related to early normal faults and syn-rift deposits. These features were recognized in the deep structure of the Pre-Andean Depressions (e.g., Salar de Punta Negra and Pedernales basins), staying hidden under the Cenozoic syn-orogenic deposits.
3. The distribution of the first-order structures exposed on both flanks of the Domeyko Cordillera is similar to the structures performed in our analog models. High-angle partially inverted normal faults are dominant in the western flank, while east-verging thrust decapitation faults are exposed on the eastern flank of the cordillera.
4. The east-verging thrust decapitation faults generated the greatest shortening and uplift on this side of the Andean forearc. Also, these thrust faults decapitated to high-angle inverted normal faults, which are well-exposed in the western flank of the Domeyko Cordillera.
5. The Domeyko Fault System geometry exposed on the western slope of the Domeyko Cordillera was compared with our analog models, being interpreted as a result of a polyphasic deformation. Thus, its kinematic nature is characterized and differentiated in three different stage. First, the Domeyko Fault System was controlled by normal faulting generated during an extensional regime. Then, their structures were inverted or partially inverted during a positive tectonic inversion, generating high-angle and west-verging inverted normal faults. Finally, these structures were decapitated and transported on hanging-walls of east-verging thrust decapitation faults.

Acknowledgments

This work was supported by EPOS-TCS-MSL-TNA access to Tectonics Modeling Laboratory of Firenze, supported by the European Community HORIZON 2020 research and innovation program under Grant 676564 and national funding EPOS ITALIA (CUP D81J11000520001). The trip and stay, in Firenze, Italy, were funded by CONICYT-PCHA/Doctorado Nacional/2018–21180396. The authors also thank Enap-Sipetrol for providing the seismic data used in the present study and to the projects LMI-COPEDIM project (IRD, France), for partial funding, and the UCN19101 project. Rodrigo Riquelme thanks the support of the FONDECYT project Grant 1170992. Fernando Martínez thanks the support of the Agencia Nacional de Investigación y Desarrollo (ANID) Research Project PCI-2019/133349-8 "Tectonostratigraphic evolution of intermontane basins related to forearc tectonic settings using the Chilean Pre-Andean Depression of the Central Andes as a case study." Finally, the authors also thank the constructive suggestions made by Daniel L. Yagupsky, Ernst Willingshofer, Laura Giambiagi, and an anonymous reviewer; special thanks to Cecilia Avila for valuable tips and reviewing the English.

Conflict of Interest

The authors declare no conflicts of interest relevant to this study.

Data Availability Statement

All the data supporting this research are available in the text. Free to download at the following link https://doi.org/10.5281/zenodo.6525575 under Creative Commons Attribution 4.0 International License.

References

Aguirre-Urreta, M. (1993). Neocomian ammonite biostratigraphy of the Andean Basin of Argentina and Chile. *Revista Espanola de Paleontologia*, *8*(1), 57–74.

Allmendinger, R., Jordan, T., Kay, S. M., & Isacks, B. (1997). The evolution of the Altiplano-Puna plateau of the Central Andes. *Annual Review of Earth and Planetary Sciences*, *25*(1), 139–174. https://doi.org/10.1146/annurev.earth.25.1.139

Amilibia, A., Sabat, F., McClay, K. R., Muñoz, J. A., Roca, E., & Chong, G. (2008). The role of inherited tectono-sedimentary architecture in the development of the central Andean mountain belt: Insights from the Cordillera de Domeyko. *Journal of Structural Geology*, *30*, 1520–1539. https://doi.org/10.1016/j.jsg.2008.08.005

Arriagada, C., Cobbold, P. R., & Roperch, P. (2006). The Salar de Atacama Basin: A record of Cretaceous to Paleogene compressional tectonics in the Central Andes. *Tectonics*, *25*(1), TC1008. https://doi.org/10.1029/2004tc001770

Arriagada, C., Roperch, P., Mpodozis, C., & Cobbold, P. R. (2008). Paleogene building of the Bolivian Orocline: Tectonic restoration of the central Andes in 2-D map view. *Tectonics*, *27*(6), TC6014. https://doi.org/10.1029/2008tc002269

Aubouin, J., Borrello, A., Cecioni, G., Charrier, R., Chotin, P., Frutos, J., et al. (1973). Esquisse paléogéographique et structurale des Andes Méridionales. *Revue de Geographie Physique et de Geologie Dynamique*, *15*(1–2), 11–72.

Bailey, C. M., Giorgis, S., & Coiner, L. (2002). Tectonic inversion and basement buttressing: An example from the central Appalachian Blue Ridge province. *Journal of Structural Geology*, *24*(5), 925–936. https://doi.org/10.1016/s0191-8141(01)00102-x

Bascuñán, S., Arriagada, C., Le Roux, J., & Deckart, K. (2015). Unraveling the Peruvian Phase of the Central Andes: Stratigraphy, sedimentology and geochronology of the Salar de Atacama Basin (22°30–23°S), northern Chile. *Basin Research*, *28*(3), 365–392. https://doi.org/10.1111/bre.12114

Bascuñan, S., Maksymowicz, A., Martínez, F., Becerra, J., Arriagada, C., & Deckart, K. (2019). Geometry and late Mesozoic-Cenozoic evolution of the Salar de Atacama Basin (22°30′–24°30′S) in the northern Central Andes: New constraints from geophysical, geochronological and field data. *Tectonophysics*, *759*, 58–78. https://doi.org/10.1016/j.tecto.2019.04.008

Bloch, W., Kummerow, J., Salazar, P., Wigger, P., & Shapiro, S. A. (2014). High-resolution image of the North Chilean subduction zone: Seismicity, reflectivity and fluids. *Geophysical Journal International*, *197*(3), 1744–1749. https://doi.org/10.1093/gji/ggu084

Bonini, M., Sani, F., & Antonielli, B. (2012). Basin inversion and contractional reactivation of inherited normal faults: A review based on previous and new experimental models. *Tectonophysics*, *522*(523), 55–88. https://doi.org/10.1016/j.tecto.2011.11.014

Boric, R., Díaz, F., & Maksaev, V. (1990). Geología y yacimientos metalíferos de la región de Antofagasta: Santiago. *Servicio Nacional de Geología y Minería, Boletín*, *40*, 246.

Boyer, S. E., & Elliot, D. (1982). Thrust system. *AAPG Bulletin*, *66*, 1196–1230. https://doi.org/10.1306/03B5A77D-16D1-11D7-8645000102C1865D

Brun, J. P. (2002). Deformation of the continental lithosphere: Insights from brittle-ductile models. *Geological Society, London, Special Publications*, *200*(1), 355–370. https://doi.org/10.1144/gsl.sp.2001.200.01.20

Butler, R. W., Tavarnelli, E., & Grasso, M. (2006). Structural inheritance in mountain belts: An Alpine–Apennine perspective. *Journal of Structural Geology*, *28*(11), 1893–1908. https://doi.org/10.1016/j.jsg.2006.09.006

Butler, R. W. H. (1987). Thrust sequences. *Journal of the Geological Society*, *144*(4), 619–634. https://doi.org/10.1144/gsjgs.144.4.0619

Cahill, T., & Isacks, B. L. (1992). Seismicity and shape of the subducted Nazca plate. *Journal of Geophysical Research*, *97*(B12), 17503–17529. https://doi.org/10.1029/92jb00493

Calderon, Y., Baby, P., Hurtado, C., & Brusset, S. (2017). Thrust tectonics in the Andean retro-foreland basin of northern Peru: Permian inheritances and petroleum implications. *Marine and Petroleum Geology*, *82*, 238–250. https://doi.org/10.1016/j.marpetgeo.2017.02.009

Cembrano, J., Lavenu, A., Yañez, G., Riquelme, R., García, M., González, G., & Hérail, G. (2007). Neotectonics. *The geology of Chile*, 231–261. https://doi.org/10.1144/goch.9

Cobbold, P. R., Rossello, E. A., Roperch, P., Arriagada, C., Gómez, L. A., & Lima, C. (2007). Distribution, timing, and causes of Andean deformation across South America. *Geological Society, London, Special Publications*, *272*(1), 321–343. https://doi.org/10.1144/gsl.sp.2007.272.01.17

Coira, B., Davidson, J., Mpodozis, C., & Ramos, V. (1982). Tectonic and magmatíc evolution of the Andes of northern Argentina and Chile. *Earth-Sciences Review, Special Issue*, *18*(18), 303–332. https://doi.org/10.1016/0012-8252(82)90042-3

Cornejo, P., Matthews, S., Mpodozis, C., Rivera, O., & Riquelme, R. (2013). Carta El Salvador, Región de Atacama. *Servicio Nacional de Geología y Minería, Carta Geológica de Chile, Serie Geología Básica*, *158*, 1.

Cornejo, P., Matthews, S., & Pérez, C. (2003). The "K-T" compressive deformation event in northern Chile (24°–27°S). *10º Congreso Geológico Chileno (Concepción)*.

Coward, M. P., Gillcrist, R., & Trudgill, B. (1991). Extensional structures and their tectonic inversion in the Western Alps. *Geological Society, London, Special Publications*, *56*(1), 93–112. https://doi.org/10.1144/gsl.sp.1991.056.01.07

Daly, M. (1989). Correlations between Nazca/Farallon plate kinematics and forearc evolution in Ecuador. *Tectonics*, *8*(4), 769–790. https://doi.org/10.1029/tc008i004p00769

del Rey, A., Deckart, K., Arriagada, C., & Martínez, F. (2016). Resolving the paradigm of the late Paleozoic–Triassic Chilean magmatism: Isotopic approach. *Gondwana Research*, *37*, 172–181. https://doi.org/10.1016/j.gr.2016.06.008

del Rey, A., Deckart, K., Planavsky, N., Arriagada, C., & Martínez, F. (2019). Tectonic evolution of the southern margin of Pangea and its global implications: Evidence from the mid Permian-Triassic magmatism along the Chilean-Argentine border. *Gondwana Research*, *76*, 301–303.

Del Ventisette, C., Bonini, M., Agostini, A., Corti, G., Maestrelli, D., & Montanari, D. (2019). Using different grain-size granularmixtures (quartz and K-feldspar sand) in analogue extensional models. *Journal of Structural Geology*, *129*, 103888. https://doi.org/10.1016/j.jsg.2019.103888

Del Ventisette, C., Bonini, M., Maestrelli, D., Sani, F., Iavarone, E., & Montanari, D. (2021). 3D-thrust fault pattern control on negative inversion: An analogue modelling perspective on central Italy. *Journal of Structural Geology*, *143*, 104254. https://doi.org/10.1016/j.jsg.2020.104254

Del Ventisette, C., Montanari, D., Bonini, M., & Sani, F. (2005). Positive fault inversion triggering 'intrusive diapirism': An analogue modelling perspective. *Terra Nova*, *17*(5), 478–485. https://doi.org/10.1111/j.1365-3121.2005.00637.x

Del Ventisette, C., Montanari, D., Sani, F., & Bonini, M. (2006). Basin inversion and fault reactivation in laboratory experiments. Tectonic inversion and structural inheritance in mountain belts. In E. Tavarnelli, R. Butler, & M. Grasso (Eds.), *Tectonic inversion processes and structural inheritance in mountain belts*. *Journal of Structural Geology* (Vol. 28, pp. 2067–2083).

Dewey, J. F., & Bird, J. M. (1970). Mountain belts and the new global tectonics. *Journal of Geophysical Research*, *75*(14), 2625–2647. https://doi.org/10.1029/jb075i014p02625

Doglioni, C., Tonarini, S., & Innocenti, F. (2009). Mantle wedge asymmetries and geochemical signatures along W- and E–NE-directed subduction zones. *Lithos*, *113*(1–2), 179–189. https://doi.org/10.1016/j.lithos.2009.01.012

Duhart, P., Muñoz, J., Quiroz, D., Mestre, A., & Varas, G. (2018). Carta Sierra Gorda, Región de Antofagasta. Servicio Nacional de Geología y Minería, Carta Geológica de Chile. In *Serie Geología Básica 198, 1 Mapa Escala 1: 100.000*. 1 CD con anexos Santiago.

Espinoza, M., Montecino, D., Oliveros, V., Astudillo, N., Vásquez, P., Reyes, R., et al. (2018). The synrift phase of the early Domeyko Basin (Triassic, northern Chile): Sedimentary, volcanic, and tectonic interplay in the evolution of an ancient subduction-related rift basin. *Basin Research*, *31*(1), 4–32. https://doi.org/10.1111/bre.12305

Espinoza, M., Oliveros, V., Vásquez, P., Giambiagi, L., Morgan, L., González, R., et al. (2021). Gondwanan inheritance on the building of the Western Central Andes (Domeyko Range, Chile): Structural and thermochronological approach (U-Pb and $^{40}Ar/^{39}Ar$). *Tectonics*, *40*(3), e2020TC006475. https://doi.org/10.1029/2020tc006475

Farías, M., Charrier, R., Comte, D., Martinod, J., & Hérail, G. (2005). Late Cenozoic deformation and uplift of the western flank of the Altiplano: Evidence from the depositional, tectonic, and geomorphologic evolution and shallow seismic activity (northern Chile at 19 30′ S). *Tectonics*, *24*(4), TC4001. https://doi.org/10.1029/2004tc001667

Folguera, A., & Ramos, V. A. (2009). The collision of the Mocha fracture zone and a new wave of orogenic uplift in the Andes (368–388S). *Lithosphere*, *1*(6), 364–369. https://doi.org/10.1130/l66.1

Fuentes, G., Martínez, F., Bascuñan, S., Arriagada, C., & Muñoz, R. (2018). Tectonic architecture of the Tarapacá Basin in the northern Central Andes: New constraints from field and 2D seismic data. *Geosphere*, *14*(6), 2430–2446. https://doi.org/10.1130/ges01697.1

Gavillot, Y., Meigs, A. J., Sousa, F. J., Stockli, D., Yule, D., & Malik, M. (2018). Late Cenozoic foreland-to-hinterland low-temperature exhumation history of the Kashmir Himalaya. *Tectonics*, *37*(9), 3041–3068. https://doi.org/10.1029/2017tc004668

Giambiagi, L., Bechis, F., García, V., & Clark, A. H. (2008). Temporal and spatial relationships of thick-and thin-skinned deformation: A case study from the Malargüe fold-and-thrust belt, southern Central Andes. *Tectonophysics*, *459*(1–4), 123–139. https://doi.org/10.1016/j.tecto.2007.11.069

González, R., Wilke, G. H., Menzies, A. H., Espinoza, F., Riquelme, R., & Herrera, C. (2015). Carta Sierra de Varas, Región de Antofagasta. Servicio Nacional de Geología y Minería, Carta Geológica de Chile. *Serie Geología Básica*, *178*(1), 100000.

Hayward, A. B., & Graham, R. H. (1996). Some geometrical characteristics of inversion. In M. A. Cooper & G. D. Williams (Eds.), *Inversion tectonics* (pp. 17–39). Geological Society Special Publication Classics.

Hubbert, M. K. (1937). Theory of scale models as applied to the study of geologic structures. *The Geological Society of America Bulletin*, *48*(10), 1459–1520. https://doi.org/10.1130/gsab-48-1459

Imber, J., Childs, C., Nell, P. A. R., Walsh, J. J., Hodgetts, D., & Flint, S. (2003). Hanging wall fault kinematics and footwall collapse in listric growth fault systems. *Journal of Structural Geology*, *25*(2), 197–208. https://doi.org/10.1016/s0191-8141(02)00034-2

Isacks, B. (1988). Uplift of the Central Andes plateau and bending of the Bolivian Orocline. *Journal of Geophysical Research*, *93*(B4), 3211–3231. https://doi.org/10.1029/jb093ib04p03211

Jain, A. K., Ahmad, T., Singh, S., Ghosh, S. K., Patel, R. C., Kumar, R., et al. (2012). Evolution of the Himalaya. *Proceedings of the Indian National Science Academy*, *78*, 259–275.

Jara, P., Likerman, J., Charrier, R., Herrera, S., Pinto, L., Villarroel, M., & Winocur, D. (2017). Closure type effects on the structural pattern of an inverted extensional basin of variable width: Results from analogue models. *Journal of South American Earth Sciences*, *87*, 157–173. https://doi.org/10.1016/j.jsames.2017.10.018

Jarrard, R. D. (1986). Relations among subduction parameters. *Review of Geophysics*, *24*(2), 217–284. https://doi.org/10.1029/rg024i002p00217

Jordan, T. E., Mpodozis, C., Muñoz, N., Blanco, N., Pananont, P., & Gardeweg, M. (2007). Cenozoic subsurface stratigraphy and structure of the Salar de Atacama Basin, northern Chile. *Journal of South American Earth Sciences*, *23*(2–3), 122–146. https://doi.org/10.1016/j.jsames.2006.09.024

Kley, J., Rossello, E. A., Monaldi, C. R., & Habighorst, B. (2005). Seismic and field evidence for selective inversion of Cretaceous normal faults, Salta rift, northwest Argentina. *Tectonophysics*, *399*(1–4), 155–172. https://doi.org/10.1016/j.tecto.2004.12.020

Kukal, Z. (1990). The rate of geological processes. *Earth-Science Reviews*, *28*(1–3), 8±284. https://doi.org/10.1016/0012-8252(90)90017-p

López, C., Martínez, F., Del Ventisette, C., Bonini, M., Montanari, D., Muñoz, B., & Riquelme, R. (2020). East-vergence thrusts and inversion structures: An updated tectonic model to understand the Domeyko Cordillera and the Salar de Atacama Basin transition in the western Central Andes. *Journal of South American Earth Sciences*, *103*(103), 102741. https://doi.org/10.1016/j.jsames.2020.102741

López, C., Martínez, F., Maksymowicz, A., Giambiagi, L., & Riquelme, R. (2019). What is the structure of the forearc region in the Central Andes of northern Chile? An approach from field data and 2-D reflection seismic data. *Tectonophysics*, *769*, 228187. https://doi.org/10.1016/j.tecto.2019.228187

Maksaev, V., & Zentilli, M. (1988). Marco metalogénico regional de los megadepósitos de tipo pórfido cuprífero del Norte Grande de Chile. In *Actas V Congreso Geológico Chileno, Santiago, Chile* (Vol. 1, pp. B181–B212).

Maksaev, V., & Zentilli, M. (1999). Fission track thermochronology of the Domeyko Cordillera, northern Chile: Implications for Andean tectonics and porphyry copper metallogenesis. *Exploration And Mining Geology*, *8*, 65–89.

Martínez, F., & Cristallini, E. (2017). The doubly vergent inverted structures in the Mesozoic basins of northern Chile (28°S): A comparative analysis from field data and analogue modeling. *Journal of South American Earth Sciences*, *77*, 327–340. https://doi.org/10.1016/j.jsames.2017.02.002

Martinez, F., Fuentes, G., Perroud, S., & Bascuñan, S. (2021). Buried thrust belt front of the western Central Andes of northern Chile: Style, age, and relationship with basement heterogeneities. *Journal of Structural Geology*, *147*, 104337. https://doi.org/10.1016/j.jsg.2021.104337

Martínez, F., Kania, J., Muñoz, B., Riquelme, R., & López, C. (2020). Geometry and development of a hybrid thrust belt in an inner forearc setting: Insights from the Potrerillos Belt in the Central Andes, northern Chile. Chile. *Journal of South American Earth Sciences*, *98*, 102439. https://doi.org/10.1016/j.jsames.2019.102439

Martínez, F., López, C., Bascuñan, S., & Arriagada, C. (2018). Tectonic interaction between Mesozoic to Cenozoic extensional and contractional structures in the Preandean Depression (23°–25°S): Geologic implications for the Central Andes. *Tectonophysics*, *744*, 333–349. https://doi.org/10.1016/j.tecto.2018.07.016

Martínez, F., López, C., & Parra, M. (2020). Effects of pre-orogenic tectonic structures on the Cenozoic evolution of Andean deformed belts: Evidence from the Salar de Punta Negra Basin in the Central Andes of Northern Chile. *Basin Research*, *32*(6), 1–22. https://doi.org/10.1111/bre.12436

Martínez, F., López, C., Parra, M., & Espinoza, D. (2019). Testing the occurrence of thick-skinned triangle zones in the Central Andes forearc: Example from the Salar de Punta Negra Basin in northern Chile. *Journal of Structural Geology*, *120*, 14–28. https://doi.org/10.1016/j.jsg.2018.12.009

Martínez, F., Muñoz, B., López, C., González, R., Parra, M., & Riquelme, R. (2021). Complex basement-involved contractional structures in the Pre-Andean basins of northern Chile: A review from seismic data. *Tectonics*, *40*(2), e2020TC006433. https://doi.org/10.1029/2020tc006433

McClay, K. R., & Buchanan, P. G. (1992). Thrust faults in inverted extensional basins. In *Thrust tectonics* (pp. 93–104). Springer.

McClay, K. R., Dooley, T., Ferguson, A., & Poblet, J. (2000). Tectonic evolution of the Sanga Sanga Block, Mahakam Delta, Kalimantan, Indonesia. *AAPG Bulletin*, *84*, 765–786.

Medwedeff, D. A. (1990). Geometry and kinematics of an active, laterally propagating wedge-thrust, Wheeler Ridge, California. *AAPG Bulletin*, *74*(CONF-900605-).

Mescua, J. F., & Giambiagi, L. B. (2012). Fault inversion vs. new thrust generation: A case study in the Malargüe fold-and-thrust belt, Andes of Argentina. *Journal of Structural Geology*, *35*, 51–63. https://doi.org/10.1016/j.jsg.2011.11.011

Montanari, D., Agostini, A., Bonini, M., Corti, G., & Ventisette, C. (2017). The Use of empirical methods for testing granular materials in analogue modelling. *Materials*, *10*(6), 635. https://doi.org/10.3390/ma10060635

Mount, V. S., Martindale, K. W., Griffith, T. W., & Byrd, J. O. D. (2011). Basement-involved contractional wedge structural style: Examples from the Hanna Basin, Wyoming. In K. McClay, J. H. Shaw, & J. Suppe (Eds.), *Thrust fault-related folding: AAPG Memoir 94* (pp. 271–281).

Mpodozis, C., Arriagada, C., Basso, M., Roperch, P., Cobbold, P., & Reich, M. (2005). Late Mesozoic to Paleogene stratigraphy of the Salar de Atacama Basin, Antofagasta, Northern Chile: Implications for the tectonic evolution of the Central Andes. *Tectonophysics*, *399*(1–4), 125–154. https://doi.org/10.1016/j.tecto.2004.12.019

Mpodozis, C., & Cornejo, P. (2012). Cenozoic tectonics and porphyry copper systems of the Chilean Andes. Chapter 14 in *Society of Economic Geologists, Inc. Special Publication* (Vol. *16*, pp. 329–360).

Mpodozis, C., Marinovic, N., Smoje, I., & Cuitiño, L. (1993). *Estudio geológico-estructural de la Cordillera de Domeyko entre Cerro Limón Verde y Sierra Mariposas, Región de Antofagasta* (Informe Registrado IR-93-04, pp. 282). Servicio Nacional de Geología y Minería.

Mpodozis, C., & Ramos, V. A. (1990). The Andes of Chile and Argentina. In *Geology of the Andes and its relation to hydrocarbon and mineral resources. Circum-Pacific Council for Energy and Mineral Resources, Houston, Texas. Earth Science Series*. (Vol. 11, pp. 59–90).

Munteanu, I., Willingshofer, E., Matenco, L., Sokoutis, D., & Cloetingh, S. (2014). Far-field contractional polarity changes in models and nature. *Earth and Planetary Science Letters*, *395*, 101–115. https://doi.org/10.1016/j.epsl.2014.03.036

Niemeyer, H., & Munizga, R. (2008). Structural control of the emplacement of the Portrerillos porphyry copper, central Andes of Chile. *Journal of South American Earth Sciences*, *26*(3), 261–270. https://doi.org/10.1016/j.jsames.2008.08.006

Niemeyer, H., & Urrutia, C. (2009). Transcurrencia a lo largo de la Falla Sierra de Varas (Sistema de fallas de la Cordillera de Domeyko), norte de Chile. *Andean Geology*, *36*(1), 37–49. https://doi.org/10.4067/s0718-71062009000100004

Oncken, O., Chong, G., Franz, G., Giese, P., Götze, H.-J., Ramos, V. A., et al. (Eds.) (2006). The Andes—Active subduction Orogeny: Berlin, Springer. *Frontiers in Earth Sciences Series*, *1*, 570.

Pace, P., Domenica, A. D., & Calamita, F. (2014). Summit low-angle faults in the Central Apennines of Italy: Younger-on-older thrusts or rotated normal faults? Constraints for defining the tectonic style of thrust belts. *Tectonics*, *33*(5), 756–785. https://doi.org/10.1002/2013tc003385

Pananont, P., Mpodozis, C., Blanco, N., Jordan, T. E., & Brown, L. D. (2004). Cenozoic evolution of the northwestern Salar de Atacama Basin, northern Chile. *Tectonics*, *23*(6). https://doi.org/10.1029/2003tc001595

Pardo-Casas, F., & Molnar, P. (1987). Relative motion of the Nazca (Farallon) and south American plates since Late Cretaceous time. *Tectonics*, *6*(3), 233–248. https://doi.org/10.1029/tc006i003p00233

Parson, T., & Thompson, G. A. (1993). Does magmatism influence low-angle normal faulting? *Geology*, *21*(3), 247–250. https://doi.org/10.1130/0091-7613(1993)021<0247:dmilan>2.3.co;2

Perez, N., Horton, B., McQuarrie, N., Stuebner, K., & Ehlers, T. (2016). Andean shortening, inversion and exhumation associated with thin-and thick-skinned deformation in southern Peru. *Geological Magazine*, *153*(5–6), 1013–1041. https://doi.org/10.1017/s0016756816000121

Ramberg, H. (1981). *Gravity, deformation and the Earth's crust in theory, experiments and geologic application* (2nd ed., p. 452). Academic Press.

Ramos, V. A. (1999). Plate tectonic setting of the Andean Cordillera. *Episodes*, *22*(3), 183–190. https://doi.org/10.18814/epiiugs/1999/v22i3/005

Ramos, V. A. (2009). Anatomy and global context of the Andes: Main geologic features and the Andean orogenic cycle. *Backbone of the Americas: Shallow subduction, plateau uplift, and ridge and terrane collision*, *204*, 31–65.

Ramos, V. A. (2010). The tectonic regime along Andes: Present-day and Mesozoic regimes. *Geological Journal*, *45*(1), 2–25. https://doi.org/10.1002/gj.1193

Reutter, K. J., Scheuber, E., & Helmcke, D. (1991). Structural evidence of orogen-parallel strike slip displacements in the Precordillera of northern Chile. *Geologische Rundschau*, *80*(1), 135–153. https://doi.org/10.1007/bf01828772

Royden, L. H., & Burchfiel, B. C. (1989). Are systematic variations in thrust-belt style related to plate boundary processes? (The Western Alps versus the Carpathians). *Tectonics*, *8*(1), 51–61. https://doi.org/10.1029/tc008i001p00051

Rubilar, J., Martínez, F., Arriagada, C., Becerra, J., & Bascuñán, S. (2017). Structure of the Cordillera de la Sal: A key tectonic element for the Oligocene-Neogene evolution of the Salar de Atacama basin, Central Andes, northern Chile. *Journal of South American Earth Sciences*, *87*, 200–210. https://doi.org/10.1016/j.jsames.2017.11.013

Sani, F., Del Ventisette, C., Montanari, D., Bendkik, A., & Chenakeb, M. (2007). Structural evolution of the Rides Prerifaines (Morocco): Structural and seismic interpretation and analogue modelling experiments. *International Journal of Earth Sciences*, *96*(4), 685–706. https://doi.org/10.1007/s00531-006-0118-2

Schellart, W. P., & Strak, V. (2016). A review of analogue modelling of geodynamic processes: Approaches, scaling, materials and quantification, with an application to subduction experiments. *Journal of Geodynamics*, *100*, 7–32. https://doi.org/10.1016/j.jog.2016.03.009

Scheuber, E., Bogdanic, T., Jensen, A., & Reuter, K. (1994). Tectonic development of the north Chilean Andes in relation to plate convergence and magmatism since the Jurassic. In K. Reuter, E. Scheuber, & P. Wigger (Eds.), *Tectonics of the Southern Central Andes* (pp. 7–22). Springer.

Scisciani, V. (2009). Styles of positive inversion tectonics in the Central Apennines and in the Adriatic foreland: Implications for the evolution of the Apennine chain (Italy). *Journal of Structural Geology*, *31*(11), 1276–1294. https://doi.org/10.1016/j.jsg.2009.02.004

Shaw, J. H., Connors, C., & Suppe, J. (2004). Seismic interpretation of contractional fault-related folds. *AAPG Studies in Geology*, *53*, 156. https://doi.org/10.1306/St531003

Somoza, R., Tomlinson, A. J., Caffe, P. J., & Vilas, J. F. (2012). Paleomagnetic evidence of earliest Paleocene deformation in Calama (~22°S), northern Chile: Andean-type or ridge-collision tectonics? *Journal of South American Earth Sciences*, *37*, 208–213. https://doi.org/10.1016/j.jsames.2012.04.001

Steinmann, G. (1929). *Geologie von Peru*. Kart Winter.

Tavarnelli, E. (1996). The effects of pre-existing normal faults on thrust ramp development: An example from the northern Apennines, Italy. *Geologische Rundschau*, *85*(2), 363–371. https://doi.org/10.1007/bf02422241

Tomlinson, A., Cornejo, P., & Mpodozis, C. (1999). Hoja Potrerillos, Región de Atacama. *Servicio Nacional de Geología y Minería, SERNAGEOMIN, Mapas Geológicos (escala 1: 100.000)*, *14*, 33.

Tomlinson, A. J., Blanco, N., Dilles, J. H., Maksaev, V., & Ladino, M. (2018). Carta Calama, Región de Antofagasta. *Servicio Nacional de Geología y Minería, Carta Geológica de Chile, Serie Geológica Básica No. 199, 1 mapa escala 1:100.000*. 1 CD con anexos.

Uyeda, S., & Kanamori, H. (1979). Back-arc opening and the mode of subduction. *Journal of Geophysical Research*, *84*(B3), 1049–1061. https://doi.org/10.1029/jb084ib03p01049

Valdiya, K. S., & Sanwal, J. (2017). Himalayan mobile Belt: The main arc. In *Developments in earth surface processes* (Vol. 22, pp. 31–109). Elsevier.

Vezzani, L., Festa, A., & Ghisetti, F. C. (2010). *Geology and tectonic evolution of the Central-Southern Apennines, Italy* (Vol. 469). Geological Society of America.

Weijermars, R. (1986). Flow behaviour and physical chemistry of bouncing putties and related polymers in view of tectonic laboratory applications. *Tectonophysics*, *124*(3–4), 325–358. https://doi.org/10.1016/0040-1951(86)90208-8

Welbon, A. I., & Butler, R. W. H. (1992). Structural styles in thrust belts developed through rift basins: A view from the western Alps. In *Structural and tectonic modelling and its application to petroleum geology* (pp. 469–479). Elsevier.

Williams, G. D., Powell, C. M., & Cooper, M. A. (1989). Geometry and kinematics of inversion tectonics. *Geological Society, London, Special Publications*, *44*(1), 3–15. https://doi.org/10.1144/gsl.sp.1989.044.01.02

Xiao, H., & Suppe, J. (1992). Origin of rollover. *AAPG*, *76*, 509–529.

Yin, A. (2006). Cenozoic tectonic evolution of the Himalayan orogen as constrained by along-strike variation of structural geometry, exhumation history, and foreland sedimentation. *Earth-Science Reviews*, *76*(1–2), 1–131. https://doi.org/10.1016/j.earscirev.2005.05.004

Yoon, M., Buske, S., Lüth, S., Schulze, A., Shapiro, S. A., Stiller, M., & Wigger, P. (2003). Along-strike variations of crustal reflectivity related to the Andean subduction process. *Geophysical Research Letters*, *30*(4), 2002GL015848. https://doi.org/10.1029/2002gl015848

Yoon, M., Buske, S., Shapiro, S. A., & Wigger, P. (2009). Reflection image spectroscopy across the Andean subduction zone. *Tectonophysics*, *472*(1–4), 51–61. https://doi.org/10.1016/j.tecto.2008.03.014

Zwaan, F., Schreurs, G., Buiter, S., Ferrer, O., Reitano, R., Rudolf, M., & Willingshofer, E. (2022). Analogue modelling of basin inversion: A review and future perspectives. *Solid Earth Discussions*, 1–84. [Preprint]. https://doi.org/10.5194/se-2022-8